



## WASHINGTON STATE FERRIES RICH PASSAGE WAKE STUDY

Brad Perfect

*Mechanical Engineering, University of Washington*

Dr Jim Thomson

*Applied Physics Laboratory, University of Washington*

Dr James Riley

*Mechanical Engineering, University of Washington*

Endicott Fay

*Washington State Department of Transportation*

September 29, 2015

## **Abstract**

Washington State Ferries operates a ferry route that travels through a 600m-wide channel called Rich Passage. The wakes generated by WSF vessels in transit are studied. We find that current protocols calling for reduced speed inside Rich Passage are effective in reducing wakes produced by Issaquah class vessels to permissible levels. For Superclass vessels, reduced speeds are not required, because the wakes from these vessels are significantly smaller. An analytic potential flow model and a Navier-Stokes RANS model were developed to help study wake generation and propagation, and their results are compared to field data obtained in Fall 2014.

## Table of Variables

Variable Name	Description
$\rho$	Seawater density. Assigned a value of $1025 \text{kg}/\text{m}^3$ for Puget Sound.
$\nu$	Kinematic viscosity of seawater. Assigned a value of $1.44 \times 10^{-6} \text{m}^2/\text{s}$ for Puget Sound.
$\vec{u}$	Cartesian velocity vector of a flow.
$\mu$	Viscosity of water.
$\vec{\omega}$	Vorticity.
$\omega$	Angular frequency of a wave.
$\{x, y, z\}$	Cartesian coordinates in the frame of the ferry boat. $x$ denotes the streamwise direction, $y$ is the crossstream direction, and $z$ is the vertical direction. The origin of the grid is located at the mass centroid in $x$ and $y$ , and at the flat sea surface in $z$ .
$k_x, k_y$	Wavenumbers associated with the analytic wake model.
$W$	Aspect ratio of a ferry boat in the analytic wake model. This is the ratio of the major to minor axis of the ellipse representing the boat. A smaller $W$ implies a more streamlined vessel.
$b$	Length of the ferry for the purpose of determining length Froude number. Commonly referred to as length at waterline.
$Fr$	Length Froude number, defined by $\frac{U}{\sqrt{gb}}$ .
$U$	Free stream velocity of flow past the ferry boat.
$\zeta$	Value of the sea surface elevation, measured as a signed perturbation from a flat surface of value 0.
$Z$	Nondimensional sea surface, defined by $\frac{4\pi^2\zeta}{b}$ .
$g$	Gravitational acceleration, given a value of $9.8 \text{m}/\text{s}^2$ .
$d$	Distance from the sailing line of a ferry. Defined as the minimum measured GPS distance between the boat and measurement buoy, interpolated in time.
$h$	Maximum wake height. This is the maximum of the absolute value of the perturbation in the free surface.
$a$	Wave amplitude, for the purpose of linear wave analysis.
$v(t)$	Sea surface velocity, for the purpose of linear wave analysis.
$T$	Wave period. When used in the numerical sense, it is defined as the time between occurrences when the surface velocity crosses from negative to positive.
$w_{m,\tau}$	Defines a generic lag window used for estimating the spectral distribution of a time signal. (See [11]).
$\Delta_t$	The sampling interval for a field instrument.

# Contents

<b>1</b>	<b>Introduction</b>	<b>7</b>
1.1	Washington State Ferries . . . . .	7
1.2	Objectives . . . . .	7
1.3	History and Previous Work . . . . .	8
1.4	Kelvin Wake Theory . . . . .	9
1.5	Experimental Design . . . . .	11
1.5.1	SWIFT Buoys . . . . .	11
1.5.2	$\mu$ SWIFT Buoys . . . . .	11
1.5.3	Shoreline Pressure Sensors . . . . .	13
1.6	Computational Design . . . . .	13
<b>2</b>	<b>Analytical Wake Modeling</b>	<b>14</b>
2.1	Underlying Assumptions . . . . .	14
2.2	Finite Pressure Disturbance Theory . . . . .	14
2.2.1	Derivation of the Sea Surface . . . . .	14
2.2.2	Pressure Distribution . . . . .	16
2.3	A Note on Stationary Phase Solutions . . . . .	17
2.4	Analytic Model Description . . . . .	18
2.5	Analytic Model Results . . . . .	19
2.5.1	Effect of Boat Shape . . . . .	19
2.5.2	Effect of Boat Velocity . . . . .	21
2.5.3	Vessel Modeling . . . . .	21
<b>3</b>	<b>Computational Results</b>	<b>21</b>
3.1	Model Description . . . . .	21
3.2	Underlying Methods . . . . .	25
3.3	Model Limitations . . . . .	25
3.3.1	Vessel Mass . . . . .	26
3.3.2	Scalability . . . . .	26
3.3.3	Numerical Dissipation . . . . .	26
3.3.4	Interface Dilution . . . . .	26
3.3.5	Turbulence Model and Boundary Layer Effects . . . . .	27
3.4	Model Results . . . . .	27
3.4.1	Transverse Wake . . . . .	27
3.4.2	Wake Height and Dissipation . . . . .	29
3.4.3	Sea Surface Time History . . . . .	30
3.4.4	Sea Surface Velocity . . . . .	30

<b>4</b>	<b>Time Domain Analysis</b>	<b>31</b>
4.1	Field Measurements . . . . .	31
4.2	Buoy Analysis Methods . . . . .	31
4.2.1	Composition of Dataset . . . . .	32
4.2.2	Extraction of Wake Events . . . . .	32
4.2.3	Filtering . . . . .	32
4.2.4	Diagonalization . . . . .	33
4.2.5	Zero Crossing and Sea Surface . . . . .	33
4.2.6	Distance Calculation . . . . .	36
4.3	Pressure Gauge Analysis . . . . .	36
4.3.1	Results . . . . .	36
4.4	Validation . . . . .	37
4.4.1	Cross-Buoy Comparison . . . . .	38
4.4.2	Group Velocity Propagation . . . . .	38
4.5	Results . . . . .	39
4.5.1	Wake Height Plots . . . . .	40
4.5.2	Boat Velocity Conclusions . . . . .	40
<b>5</b>	<b>Frequency Domain Analysis</b>	<b>40</b>
5.1	Methods . . . . .	40
5.2	Background Spectral Analysis . . . . .	41
5.2.1	SWIFT Background Spectra . . . . .	41
5.2.2	$\mu$ SWIFT Background Spectra . . . . .	42
5.3	Side by Side Buoy Comparison: A Case Study . . . . .	43
5.3.1	Background Signal Spectral Estimates . . . . .	43
5.3.2	Wake Signal Spectral Estimates . . . . .	45
5.3.3	Cross Spectra . . . . .	48
5.4	Maximum Wake Height Frequency . . . . .	50
5.5	Frequency Domain Conclusions . . . . .	52
<b>6</b>	<b>Model Comparison and Validation</b>	<b>52</b>
6.1	Wake Height Plots . . . . .	52
6.2	Lagrangian Tracking Comparisons . . . . .	53
<b>7</b>	<b>Conclusions</b>	<b>55</b>
7.1	Summary . . . . .	55
7.2	Vessel Speed Recommendations . . . . .	55
7.3	Conclusions from Modeling . . . . .	55
7.4	Possible Extensions and Future Work . . . . .	55
<b>8</b>	<b>Acknowledgements</b>	<b>56</b>

<b>9</b>	<b>Appendix</b>	<b>56</b>
9.1	Rich Passage Depth Chart . . . . .	56
9.2	Processed Pressure Gauge Data . . . . .	56
9.3	Lagrangian Tracking Comparison Plots . . . . .	62
9.4	Statistical Methods . . . . .	68

# 1 Introduction

## 1.1 Washington State Ferries

Washington State Ferries (WSF) operates a fleet of 22 vessels in the Puget Sound region of Washington and British Columbia. It is the largest ferry system in the United States and services the highest volume of automobiles of any ferry service in the world. The Seattle-Bremerton route, servicing 2.33 million passengers and 642,000 vehicles per year [13], is the primary subject of the current study. In the Rich Passage section of the route, denoted by the yellow box in Fig. 1, WSF Issaquah Class ferries are currently self-limiting vessel speed to 12 knots due to concerns over damage to beachfront properties, which were voiced by the property owners. This is considerably below the 16.5 knot standard operating speed, and results in added annual fuel costs on the order of \$400,000.



Figure 1: Ferry route map, with the Rich Passage area boxed.

## 1.2 Objectives

The purpose of this study is to

1. Develop criteria for appropriate vessel speed limitations through models and data
2. Develop and validate modeling capabilities for WSF vessel wakes
3. Study wake development and propagation in a variety of empirical and modeled scenarios.

### 1.3 History and Previous Work

The question of wakes in Rich Passage dates to the early 1990's, when Passenger-Only Fast Ferry (POFF) routes through the area were noted to cause excessive wakes. In the summer of 1990, residents successfully lobbied for a 12 knot speed limit for ferries within the channel. The POFF service, after several years of attempts to minimize wake without sacrificing speed, was cancelled due to expenses in 2003[6]. In 2010, Kitsap Transit purchased the Rich Passage I, a double-hulled POFF to service the Seattle-Bremerton route. The hull shape was specifically engineered to create minimal wake. Kitsap Transit, a regional public transit agency that is separate from WSF, hired the consulting firm Golder and Associates to study the operation of the Rich Passage I and report on the results. Golder and Associates concluded that the Rich Passage I meets wake height guidelines specified by

$$H = \begin{cases} H < 0.2 & T \leq 3.5 \\ H < 1.16T^{-1.4} & T > 3.5 \end{cases} \quad (1)$$

where H is the the wake height in meters measured 300m from the sailing line of the vessel, and T is the wake period in seconds. This criterion is based on the observation that low-frequency waves contain more erosive potential because of their higher energy flux, and therefore have a more restrictive associated height limit. The morphological shoreline response was largely inconclusive [3]. It is important to note, however, that the Rich Passage I study, and associated wake criteria and conclusions, are specific to Kitsap Transit's operations, and have no official bearing on WSF operations. Furthermore, the Golder and Associates study included only the unique hull design of the Rich Passage I and did not consider car ferries, as this study does.

A preliminary car ferry wake study was carried out in the spring of 2014 by Jake Dossett, as his senior oceanography project. Due to windy conditions and insufficient ferry-tracking capabilities, results were inconclusive, but several of the methods developed in his term paper [4] were applied in the present study.

WSF commissioned a similar study of the car ferry fleet in 1985 [9]. This study involved Issaquah, Superclass, and Evergreen class models in open water in Puget Sound. No modeling efforts accompanied this study; rather, a suite of spar bouys were used to measure the vertical position of the sea surface.

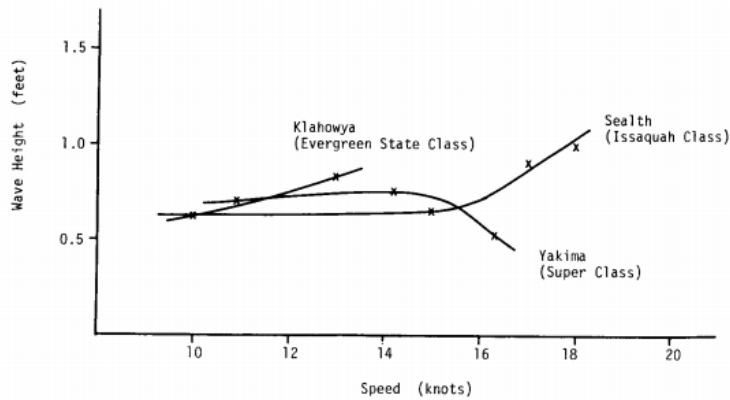


Figure 2: Results from the 1985 WSF study. All data points were taken at 600ft from the sailing line. Fit lines are hand drawn, and standard deviations for each data point are significant, but were not shown in the study report.

The results, summarized by Fig. 2, establish that the Super class vessel wakes grow at a much slower rate as vessel speed increases when compared to the Issaquah class. A drawback of this study was the sparse availability of data, difficulty in distinguishing wakes from oceanic noise, and uncertainty in measuring distance from sailing line, making the conclusions difficult to quantify. Sailing line distances were measured using real-time by-hand triangulation and analyzing aerial photographs taken during the experiment.

Concurrent to this study, a pair of acoustic wave and current (AWAC) monitors were placed in Rich Passage to measure natural wave action. The natural wave height results may serve as a rough comparison to ferry wakes, though the ferry wakes are much more regular. Fig. 3 reports the significant wave height from 16 September, 2014 to 18 November 2014. The natural significant wave height rarely exceeds 30cm, and exceptions to this are typically associated with storm events.

#### 1.4 Kelvin Wake Theory

The present study is a specific extension of the larger field of ship wakes. A wake is a disturbed region in a medium caused by flow past a solid object. In the special case of an air-water interface (characterized by a free surface between two incompressible fluids of different densities), an easily recognizable pattern is produced. This pattern is referred to as a Kelvin wake, named for Willam Thomson, the Lord Kelvin[15]. In 1887, Kelvin showed that the wake of a point pressure moving across a fluid surface may be described analytically. Kelvin’s derivation, which is not discussed here<sup>1</sup>, is based in potential flow theory. Potential flow describes the special case of the

<sup>1</sup>The interested reader is referred to *Water Waves, by JJ Stoker [12]*

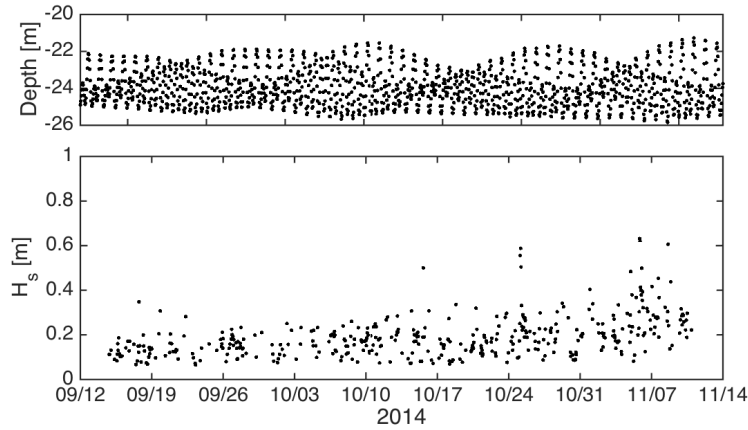


Figure 3: The time-dependent significant wave heights, as measured by the AWAC monitors in Rich Passage. High peaks typically indicate storm events. The top plot gives the height of the water column above the AWAC, which varies tidally.

Navier-Stokes equations,

$$\frac{\partial}{\partial t}(\rho \vec{u}) + \rho(\vec{u} \cdot \nabla \vec{u}) = \mu \nabla^2 \vec{u} + \rho \vec{g} \quad \nabla \cdot \vec{u} = 0, \quad (2)$$

subject to the restrictions

$$\mu = 0 \quad \text{and} \quad \vec{\omega} = \nabla \times \vec{u} = 0, \quad (3)$$

where  $\mu$  is the viscosity of the flow and  $\vec{\omega}$  is the vorticity. His result quantified a well-known wake structure that had previously only been understood empirically. A wake in water consists of two main components – the transverse wake, which follows directly behind the moving disturbance and in the same direction, and the diverging wake, which forms the characteristic V shape.

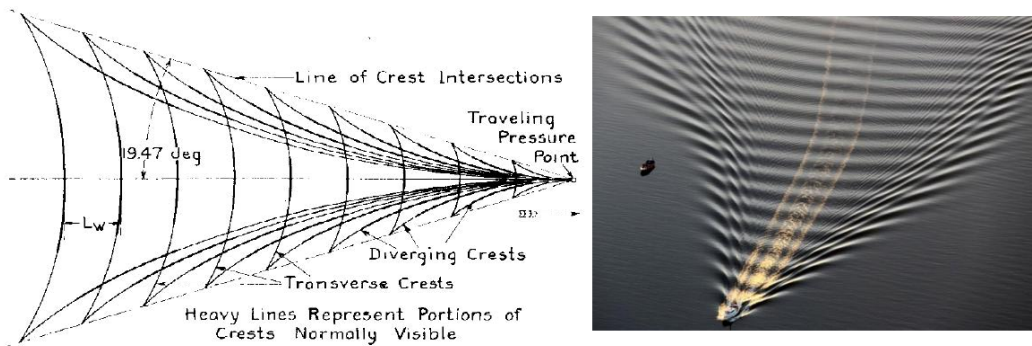


Figure 4: Left: A schematic drawing of a Kelvin wake. Right: an aerial image of a ship wake.

These two components of the wake are superimposed to produce the entire wake, as shown in Fig. 4. Kelvin’s wake theory is useful in obtaining an analytical solution to a ship wake, but is limited by the restrictions of potential flow outlined in Eq. (3) and for a point source pressure distribution. Specifically, the effects of turbulence and frictional losses cannot be taken into account. The pressure distribution restriction is relaxed in 2.2 below. The fundamental wake structure and scaling obtained from Kelvin Wake theory will be the basis for assessing the basic correctness of models and measurement, as well as providing several key validations.

## 1.5 Experimental Design

In order to assess ferry wakes in-situ, data were obtained using a suite of instrumentation on 17 September 2014 and 18 November 2014. Eight  $\mu$ SWIFT buoys, four SWIFT buoys, and two AQD pressure plates were deployed. The buoys collected GPS location and velocity data while freely floating, and the pressure plates collected time histories of the pressure 2-4m below the surface along the shoreline. The ferries whose wakes were measured were the Kaleetan (Super class), Sealth (Issaquah class), Cathlamet (Issaquah class), and Kitsap (Issaquah class). M/V Sealth has an identical hull to the other Issaquah class vessels, but has a smaller vehicle capacity, which would reduce the fully loaded weight of the vessel. However, because the operating mass of each vessel varies with each transit depending on the cargo, the Issaquah class vessels will all be considered identical.

APL staff and researchers were based on the R/V Jack Robertson, with a small rigid hull support vessel (Achilles) deployed from the Jack Robertson. The buoys were deployed from either the Jack Robertson or the Achilles in advance of the passing WSF vessels and allowed to float freely, while logging data on board.

### 1.5.1 SWIFT Buoys

SWIFT (Surface Wave Instrument Float with Tracking) buoys are free drifting systems to measure waves, winds, turbulence, and ambient noise at the ocean surface [14]. Fig. 5 shows the appearance and instrumentation of a SWIFT buoy. Sampling was at 4Hz for this project. SWIFT buoys log data on board for approximately 10-minute intervals, and then switch off for several minutes to perform onboard data processing. Because these buoys are designed for long-term deployments, the duty cycle in data recording cannot be easily controlled. Approximately 35% of wake events occur during onboard processing and are not recorded.

### 1.5.2 $\mu$ SWIFT Buoys

The  $\mu$ SWIFT is a smaller, less expensive version of the SWIFT, developed at the University of Washington’s Applied Physics Laboratory (APL). Fig. 6 is an image of a typical  $\mu$  SWIFT buoy. A QStarz BT-Q1000eX GPS logger is secured inside a

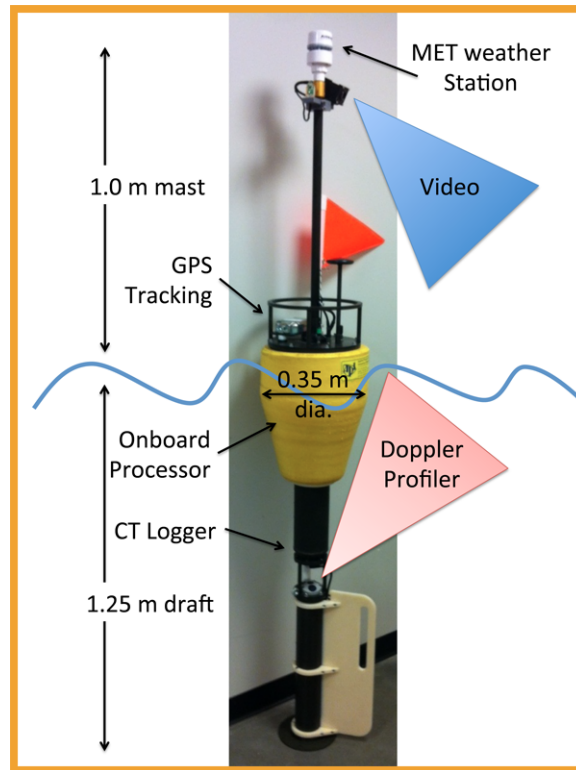


Figure 5: Image and schematic of the SWIFT data buoy. A fleet of 4 such buoys were used.

Nalgene bottle and fitted with PVC, weights, and foam for flotation and stability. The exact arrangement of stability components varied buoy-to-buoy. Data logging frequency ranges from 1 Hz to 10 Hz, depending on the selected setting. Data taken at 5 and 10 Hz were used for this study. Unlike the SWIFT, the  $\mu$ SWIFT is intended for short deployments, and recording is continuous throughout the day.

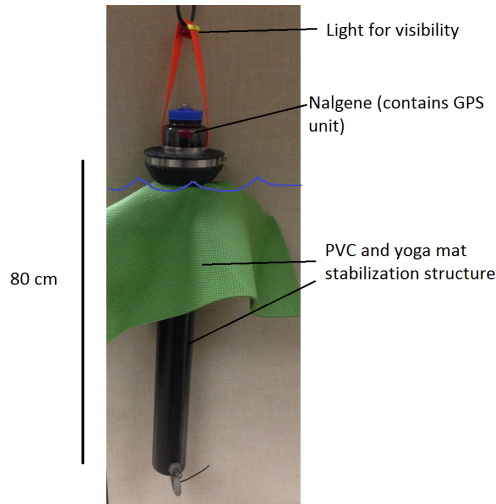


Figure 6: Image and schematic of the  $\mu$ SWIFT data buoy. A fleet of 9 such buoys were used.

### 1.5.3 Shoreline Pressure Sensors

The Nortek Aquadopp profiler is a bottom-mounted sensor designed to measure the current profile in water using Doppler imaging [10]. It is also fitted with a hydrostatic pressure sensor, which is the functionality that is used in this study. The pressure sensor is piezoresistive and logs the hydrostatic pressure for a working depth of 0-100 meters. The reported accuracy and resolution are 0.25% and 0.005% of full scale. The pressure was recorded at 8Hz for the entire multiple-hour deployment. Fig. 7 is an image of a deployed Aquadopp. Two Aquadopps were deployed on the sea floor in shallow water near the northeast shoreline of Rich Passage.

## 1.6 Computational Design

The open source software OpenFOAM was used for computational modeling. It contains a Navier-Stokes model developed to track the free surface interface between air and water. CAD models for the Issaquah and Super class hulls were obtained from WSF to use in this model. The motion of the vessel was tracked in heave and pitch, and the mesh updated to account for such motion. The wake pattern is determined by calculating the air-water interface and measuring the vertical coordinates of that surface. The model is allowed to evolve in time until a wake pattern develops, as shown in Fig. 8. The solver permits the vessel to heave and pitch, and thus produces an inherently unsteady solution, but the heave and pitch are small enough to yield a solution that can qualitatively be considered to be steady state.

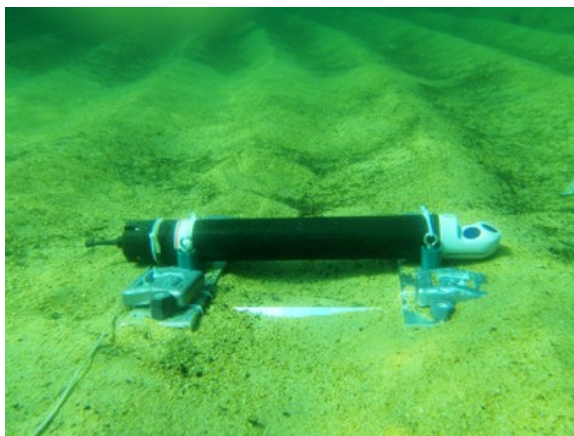


Figure 7: Image of an AQD. Two of these were used. Image from Nortek USA, the instrument’s manufacturer. The right side of the AQD is the doppler head, which emits acoustic waves used to profile the current. The bulk of the device is used for onboard processing and storage.

## 2 Analytical Wake Modeling

### 2.1 Underlying Assumptions

As stated above in Eq. (2) and Eq. (3), this analysis is limited to inviscid and irrotational flow ( $\mu = 0, \nabla \times \vec{u} = 0$ ). The effects of turbulent dissipation, turbulent and laminar boundary layers, surface tension, and interfacial friction are neglected. Of these ignored effects, the boundary layer development on the vessel hull is likely the largest component. Furthermore, the approximations used below are only valid for elliptical Gaussian pressure fields, so the intricate hull shapes of the WSF boats cannot be represented in detail.

### 2.2 Finite Pressure Disturbance Theory

Whereas Kelvin’s original derivation was for a Dirac delta function moving along the surface of the water, a series of papers in 2013-14 published by Darmon, Benzaquen, and Raphael[2, 5] treat the case of a Gaussian pressure distribution moving along the surface of a fluid. Their theory is limited to elliptical pressure distributions in deep water. The eccentricity factor  $W$  describes the aspect ratio  $0 < W < 1$  of the pressure distribution (where 1 is circular and smaller  $W$  implies a more streamlined distribution). By choosing the correct eccentricity factor, we may roughly model the shape of a boat.

#### 2.2.1 Derivation of the Sea Surface

The sea surface generated by a moving pressure distribution  $p(x, y)$  is given by [5]

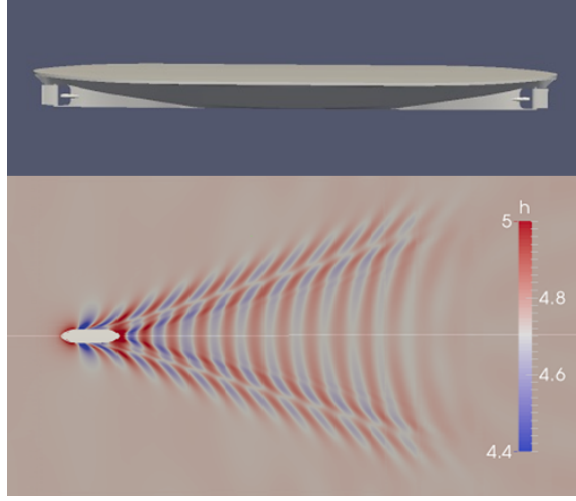


Figure 8: Top: a CAD model of an Issaquah hull. Bottom: a wake pattern generated by allowing water to flow past the hull model

$$\zeta(x, y) = -\lim_{\epsilon \rightarrow 0} \int_{-\infty}^{\pi/2} \int_0^{\infty} \frac{dk_x dk_y}{4\pi^2 \rho} \frac{k \hat{p}(k_x, k_y) e^{-i(k_x x + k_y y)}}{\omega(k)^2 - U^2 k_x^2 + 2i\epsilon U k_x}$$

where  $\hat{p}(k_x, k_y)$  is the Fourier transform of the pressure distribution  $p$ ,  $\rho$  is the constant fluid density,  $\omega(k)$  is the surface wave phase speed,  $k = \sqrt{k_x^2 + k_y^2}$ , and  $U$  is the pressure distribution's constant forward velocity. Following the method developed by Darmon et al., we apply the nondimensionalization conditions for a boat of length  $b$ :

$$X = \frac{x}{b} \quad Y = \frac{y}{b} \quad K_X = k_x b \quad K_Y = k_y b \quad Z = \frac{4\pi^2 \zeta}{b} \quad \hat{P} = \frac{\hat{p}}{\rho g b^3} \quad \tilde{\epsilon} = \epsilon \sqrt{\frac{b}{g}}$$

Using this, we obtain

$$\begin{aligned} \frac{Z(X, Y)b}{4\pi^2} &= -\lim_{\tilde{\epsilon} \rightarrow 0} \int_{-\pi/2}^{\pi/2} \int_0^{\infty} \frac{dK_X dK_Y}{4\pi^2 b^2 \rho} \frac{\frac{K}{b} \rho g b^3 \hat{P}(K_X, K_Y) e^{-i(K_X X + K_Y Y)}}{\frac{gK}{b} - U^2 \frac{K_X^2}{b^2} + 2i\tilde{\epsilon} \sqrt{\frac{g}{b}} U \frac{K_X}{b}} \\ Z(X, Y) &= -\lim_{\tilde{\epsilon} \rightarrow 0} \int_{-\pi/2}^{\pi/2} \int_0^{\infty} \frac{dK_X dK_Y}{b^4 \rho} \frac{K \rho g b^3 \hat{P}(K_X, K_Y) e^{-i(K_X X + K_Y Y)}}{\frac{gK}{b} - U^2 \frac{K_X^2}{b^2} + 2i\tilde{\epsilon} \sqrt{\frac{g}{b^3}} U K_X} \\ &= -\lim_{\tilde{\epsilon} \rightarrow 0} \int_{-\pi/2}^{\pi/2} \int_0^{\infty} \frac{dK_X dK_Y K \hat{P}(K_X, K_Y) e^{-i(K_X X + K_Y Y)}}{K - Fr^2 K_X^2 + 2i\tilde{\epsilon} Fr K_X} \end{aligned}$$

We now define the elliptic transform

$$X = \check{R} \cos \check{\varphi} \quad Y = W \check{R} \sin \check{\varphi} \quad K_X = \check{K} \cos \check{\theta} \quad K_Y = W^{-1} \check{K} \sin \check{\theta},$$

where the aspect ratio  $W$  is in the denominator for the  $Y$ -direction wavenumber. Applying this transformation, we obtain

$$Z(\check{R}, \check{\varphi}) = - \lim_{\check{\varepsilon} \rightarrow 0} \int_{-\pi/2}^{\pi/2} \int_0^{\infty} \frac{\check{K}}{W} d\check{K} d\check{\theta} \frac{\check{K} \sqrt{\cos^2 \check{\theta} + W^{-2} \sin^2 \check{\theta}} \check{P}(\check{K}) W e^{-i\check{K}\check{R}(\cos \check{\varphi} \cos \check{\theta} + \sin \check{\varphi} \sin \check{\theta})}}{\sqrt{\cos^2 \check{\theta} + W^{-2} \sin^2 \check{\theta} - Fr^2 \check{K}^2 \cos^2 \check{\theta} + 2i\check{\varepsilon} Fr \check{K} \cos \check{\theta}}}, \quad (4)$$

where the Jacobian of the coordinate transformation is  $\frac{\check{K}}{W}$ , and  $\check{P}(\check{K}) = \frac{\hat{P}(K_X, K_Y)}{W}$  to account for the reduced dimension. Simplifying,

$$Z(\check{R}, \check{\varphi}) = - \lim_{\check{\varepsilon} \rightarrow 0} \int_{-\pi/2}^{\pi/2} \int_0^{\infty} \check{K} d\check{K} d\check{\theta} \frac{\sqrt{W^2 \cos^2 \check{\theta} + \sin^2 \check{\theta}} \check{P}(\check{K}) e^{-i\check{K}\check{R} \cos(\check{\theta} - \check{\varphi})}}{\sqrt{W^2 \cos^2 \check{\theta} + \sin^2 \check{\theta} - W Fr^2 \check{K} \cos^2 \check{\theta} + 2i\check{\varepsilon} Fr W \cos \check{\theta}}}. \quad (5)$$

The Sokhotski-Plemelj formula[1] states that for a function  $f(x)$  with Cauchy principal value  $Q$ ,

$$\lim_{\check{\varepsilon} \rightarrow 0} \int_a^b \frac{f(x)}{x \pm i\check{\varepsilon}} dx = \mp i\pi f(0) + Q \int_a^b \frac{f(x)}{x} dx.$$

We can fit Eq. (5) into this form, using

$$x = \frac{\sqrt{W^2 \cos^2 \check{\theta} + \sin^2 \check{\theta}} - W Fr^2 \check{K} \cos^2 \check{\theta}}{2FrW \cos \check{\theta}} \quad dx = -\frac{Fr \cos \check{\theta}}{2} d\check{K}$$

$$f(x) = \check{K} \frac{\sqrt{W^2 \cos^2 \check{\theta} + \sin^2 \check{\theta}} \check{P}(\check{K}) e^{-i\check{K}\check{R} \cos(\check{\theta} - \check{\varphi})}}{Fr^2 W \cos^2 \check{\theta}}.$$

The zero point in  $f$  is determined uniquely by  $\check{K}$  since it is the only independent variable. Therefore, we designate

$$\check{K}_0 \equiv \frac{\sqrt{W^2 \cos^2 \check{\theta} + \sin^2 \check{\theta}}}{W Fr^2 \cos^2 \check{\theta}}$$

by solving  $x = 0$  in  $\check{K}$ . It is argued in [2] that  $Q \int_a^b \frac{f(x)}{x} dx$  is a rapidly decreasing function that can be ignored. Therefore, the sea surface is given by

$$Z(\check{R}, \check{\varphi}) \approx i\pi \int_{-\pi/2}^{\pi/2} \frac{\check{P}(\check{K}_0) \left( W^2 \cos^2 \check{\theta} + \sin^2 \check{\theta} \right) e^{-i\check{K}_0 \check{R} \cos(\check{\theta} - \check{\varphi})}}{W^2 Fr^4 \cos^4 \check{\theta}} d\check{\theta} \quad (6)$$

### 2.2.2 Pressure Distribution

The pressure distribution is assumed to be of the form

$$P(x, y) = A e^{-\left(\frac{x\pi}{b}\right)^2 - \left(\frac{y\pi}{Wb}\right)^2}. \quad (7)$$

Then, in nondimensional and Fourier transformed coordinates,

$$P(X, Y) = \frac{\pi m}{\rho b^3} e^{-\left(\frac{x\pi}{b}\right)^2 - \left(\frac{y\pi}{Wb}\right)^2}$$

$$\hat{P}(K_X, K_Y) = \frac{m}{2\pi \rho b^3} e^{-\frac{1}{4\pi^2}(K_X^2 + W^2 K_Y^2)}$$

$$\check{P}(\check{K}) = \frac{m}{2\pi \rho b^3} e^{-\frac{\check{K}^2}{4\pi^2}}$$

The  $b$  and  $W$  parameters may be tuned to approximate the geometry of the physical hulls. Fig. 9 shows such a distribution. Unfortunately, due to the asymptotic nature of the Gaussian pressure distribution, it is not possible to construct such a hull model for computational study. In order to avoid the ship being underwater, and offset must be introduced to the model, which is not attainable in the analysis in Section 2.2.1.

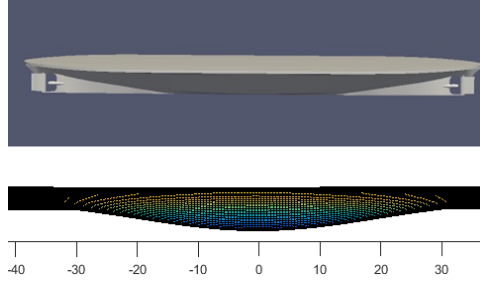


Figure 9: Comparison of a CAD model of an Issaquah vessel with a pressure distribution with parameters  $b = 94.25$  and  $W = 0.223$ .

### 2.3 A Note on Stationary Phase Solutions

A classic method of solving this problem, and the method used by Darmon et al. in [2, 5], is to apply the method of stationary phase. For an integral of the form

$$I = \int F(\theta) e^{i\phi(\theta)} d\theta, \quad (8)$$

if  $\phi(\theta)$  is sufficiently large, the integrand will undergo rapid oscillations that have a cancellation effect upon integration. Applying the stationary phase approximation [12] to Eq. (8), we obtain

$$I = \sum_m \frac{\sqrt{2\pi} F(\theta_m)}{\sqrt{|\phi''(\theta_m)|}} e^{i\phi(\theta_m) \pm \frac{i\pi}{4}} \quad (9)$$

where  $\theta_m$  are the points of stationary phase (defined by satisfying  $\frac{d\phi(\theta)}{d\theta} = 0$ ), and  $\phi''$  is the second derivative of  $\phi$ .

In the ship wake problem, we find that the number of zeros in the phase function from Eq. (9), and therefore the number of points of stationary phase in the range  $[-\frac{\pi}{2}, \frac{\pi}{2}]$ , depends on the location in the wake. Within a cone with a half angle of 19.47 degrees ( $\arcsin \frac{1}{3}$ ), trailing the vessel, there are two zeroes. The cone half angle is known as the Kelvin Angle. These zeros correspond to two separate wake patterns. One zero produces the transverse wake pattern, in which long, relatively straight waves follow the vessel and propagate at the same speed. In deep water, the dispersion relation for gravity waves dictates that the wavelength of these waves depends on the vessel speed. The other zero produces the diverging wake, which travels at an angle relative to the boat's motion, and is typically the more energetic component of the wake, especially at high boat velocity.[13]

On the boundary of the cone, there is a single zero, which also corresponds to an inflection point, and therefore, the results of the stationary phase method would produce a division by zero. To avoid this, a higher order term must be taken instead. Finally, outside of the cone, there are no zeros, corresponding to undisturbed water.

## 2.4 Analytic Model Description

A cartesian grid  $[\mathbf{X}, \mathbf{Y}]$  is formed, and each  $(X, Y)$  is transformed into the elliptical coordinates used in Eq. (6). Then, for each transformed point, the integral is evaluated numerically with a straight forward rectangular algorithm. The stationary phase approximation, which is used for all analysis in [2, 5], is not sufficient to properly resolve wake height and boundary behavior, because real wakes are not strictly confined by the Kelvin Angle. Furthermore,  $\phi(\theta)$  is not sufficiently large to permit the stationary phase approximation to satisfy the required accuracy for this study. The shortcomings of using the stationary phase method are demonstrated in Fig. 10.

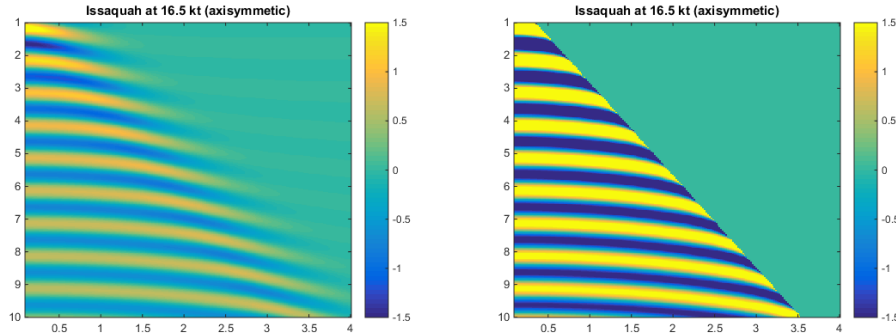


Figure 10: Comparison of a numerically evaluated wake (left) with the results of using the stationary phase approximation (right). Stationary phase is insufficient

In order to ensure the accuracy of the numerical integration, convergence studies were conducted for the  $d\theta$  parameter in the integration. Fig. 11 tracks the conver-

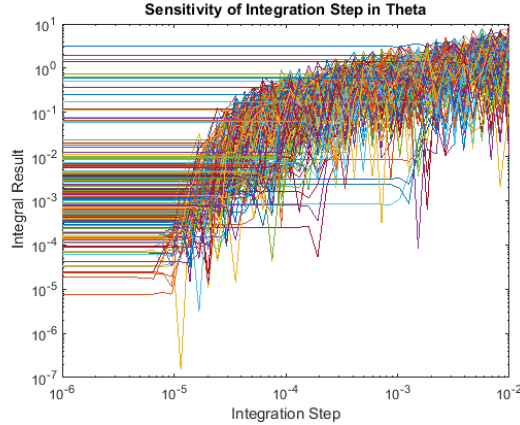


Figure 11: The value of Eq. (6) evaluated for varying  $d\theta$  values. Each line indicates a random selection for points on the surface  $(R, \varphi)$ .

gence of the sea surface value of several randomly chosen points as the integration step is varied. A trend of  $d\theta_{\text{converged}} \propto \frac{1}{R}$  emerged, where  $R$  is the radial distance from the vessel. In performing integrations,  $d\theta$  was varied locally to ensure the most computationally efficient choice that also guaranteed a result within 1% of the converged value for Eq. (6).

The parameters being varied in this study are the length Froude number,  $Fr \equiv \frac{V}{\sqrt{gb}}$ , and the aspect ratio of the pressure ellipse,  $W$ . In dimensional variables, this is the equivalent of varying boat shape and speed.

## 2.5 Analytic Model Results

Starting from Eq. (6), we may expand  $Z$  and  $\hat{P}$  into their full forms:

$$Z(R, \varphi) = \frac{4\pi^2 \zeta(R, \varphi)}{b} \quad \hat{P} = \frac{\hat{p}}{\rho g b^3}.$$

The process of performing a two-dimensional Fourier transform of the pressure changes the dimensions of pressure from Pascals to Newtons, reflecting the total pressure force, rather than the local pressure. The resulting  $\hat{P}$  takes the form of an exponential function multiplied by  $\frac{mg}{\rho g b^3}$ , where  $mg$  represents the boat's weight.

### 2.5.1 Effect of Boat Shape

If  $Fr, b$ , and  $m$  are held constant, we may explore the sea surface dependence on aspect ratio  $W$ . Increasing the aspect ratio of the boat has two effects. First, the wake height increases, and second, the wake structure appears more undeveloped, in the sense that the wake structure mimics that of a boat moving at a lower speed. The pressure distribution function is scaled to maintain constant mass when  $W$  is

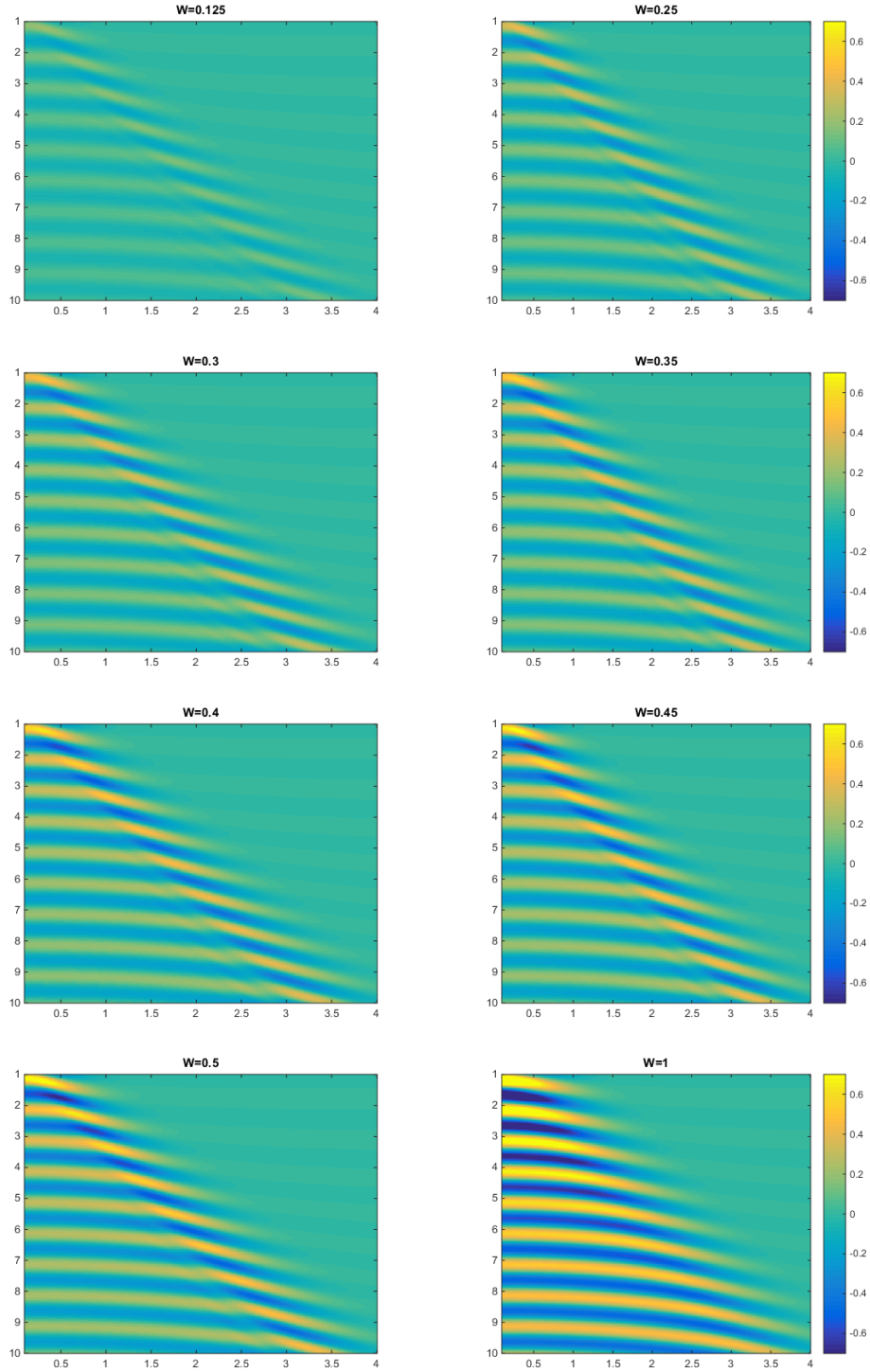


Figure 12: Various analytic wake patterns for constant  $Fr = 0.3765$ ,  $b = 52m$ ,  $m = 3.36 \times 10^6 kg$ . The  $x$  and  $y$  spatial axes are normalized by  $\frac{1}{2\pi Fr^2 b}$

varied. Fig. 12 shows that for large  $W$ , the transverse and diverging wakes merge into one entity, which is characteristic of boats moving at a lower Froude number. The eight panels show wake patterns produced for a range of aspect ratios  $W$ . In each image, the boat is located just above the top left corner and the image exhibits symmetry about the  $y$ -axis. For comparison, the  $W = 0.3$  image corresponds to a velocity of  $8.5m/s$  in Fig. 13.

### 2.5.2 Effect of Boat Velocity

Because of the dependence of the sea surface on boat length  $b$ , velocity is used as a proxy for manipulating the Froude number while maintaining constant boat length  $b$ . The Froude number is directly proportional to the boat velocity. As we can see visually in Fig. 13, the structure of the wake pattern shifts from relatively dominant transverse wakes to dominant diverging wakes. Fig. 15 explores how the maximum wake height at a given lateral distance from the sailing line changes as we vary that distance. Note that the structure of the curve changes between the lower two velocities. This corresponds to the visual rift between the transverse and diverging wakes that appears between  $7m/s$  and  $8m/s$  in Fig. 13. We can further investigate this apparent shift in Fig. 14. The best fit for maximum wave height  $h$  at a distance  $d$  from the sailing line has a best fit of

$$h(d) \propto d^{-0.23} \tag{10}$$

when the diverging wake dominates, and a best fit of

$$h(d) \propto d^{-0.4} \tag{11}$$

in the limit of a dominant transverse wake.

### 2.5.3 Vessel Modeling

In order to address the physical wakes, the model parameters were chosen to represent an Issaquah class and a Super class vessel. Using the available vessel dimensions, mass, and CAD models, pressure distributions such as Fig. 9 were created. The resulting wake profiles, shown in Fig. 16, were highly dependent on the  $b$  parameter, but in all cases, the Issaquah class model produced much larger wakes than the Super class model.

## 3 Computational Results

### 3.1 Model Description

A CAD model of a ferry boat is placed in an air/water flow moving at a specified velocity  $U$ . The flow structure is allowed to develop in the time domain, and the

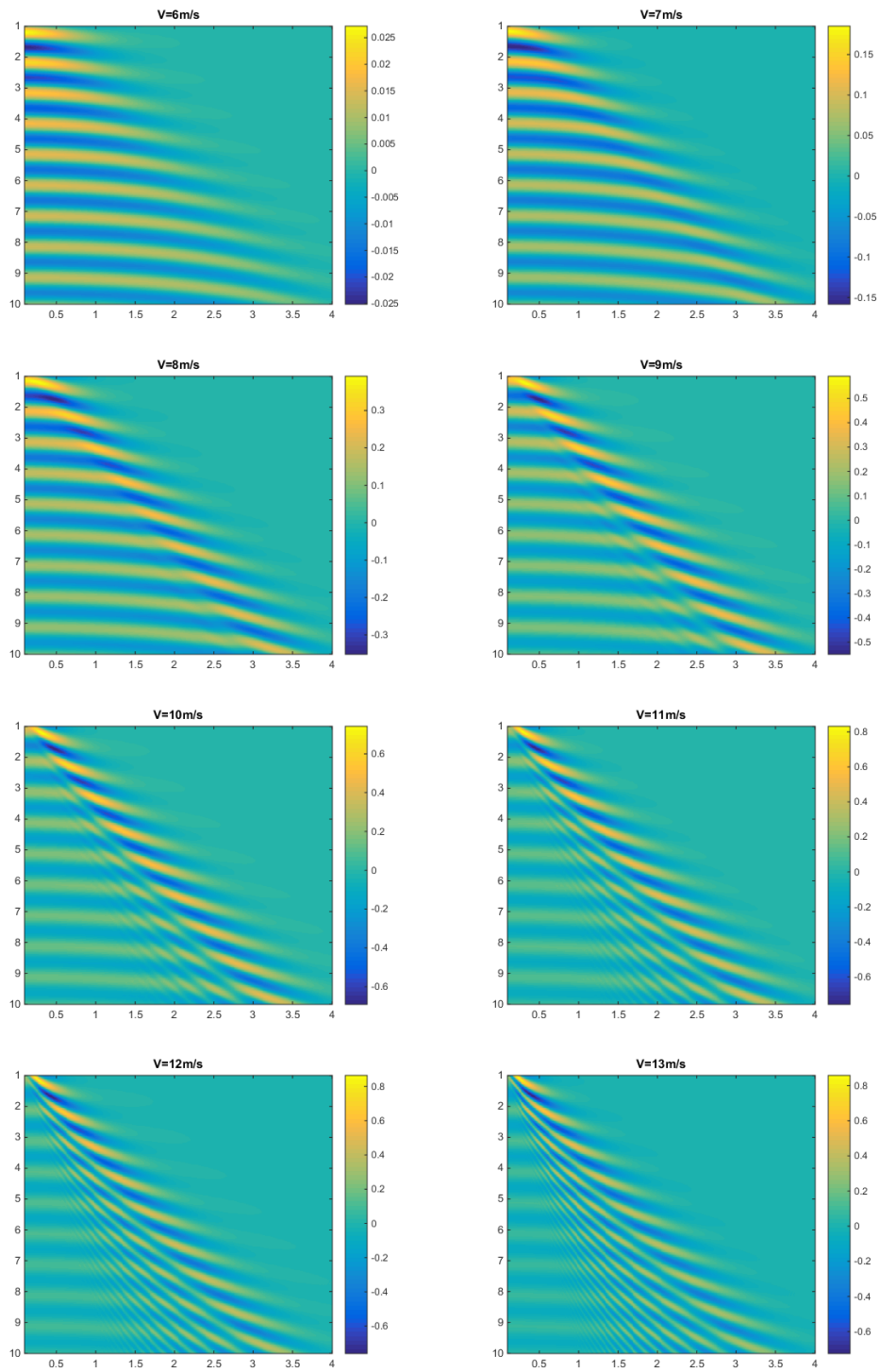


Figure 13: Various analytic wake patterns for constant  $b = 52m$ ,  $m = 3.36 \times 10^6 kg$ ,  $W = 0.3$ . The  $x$  and  $y$  spatial axes are normalized by  $\frac{1}{2\pi Fr^2 b}$

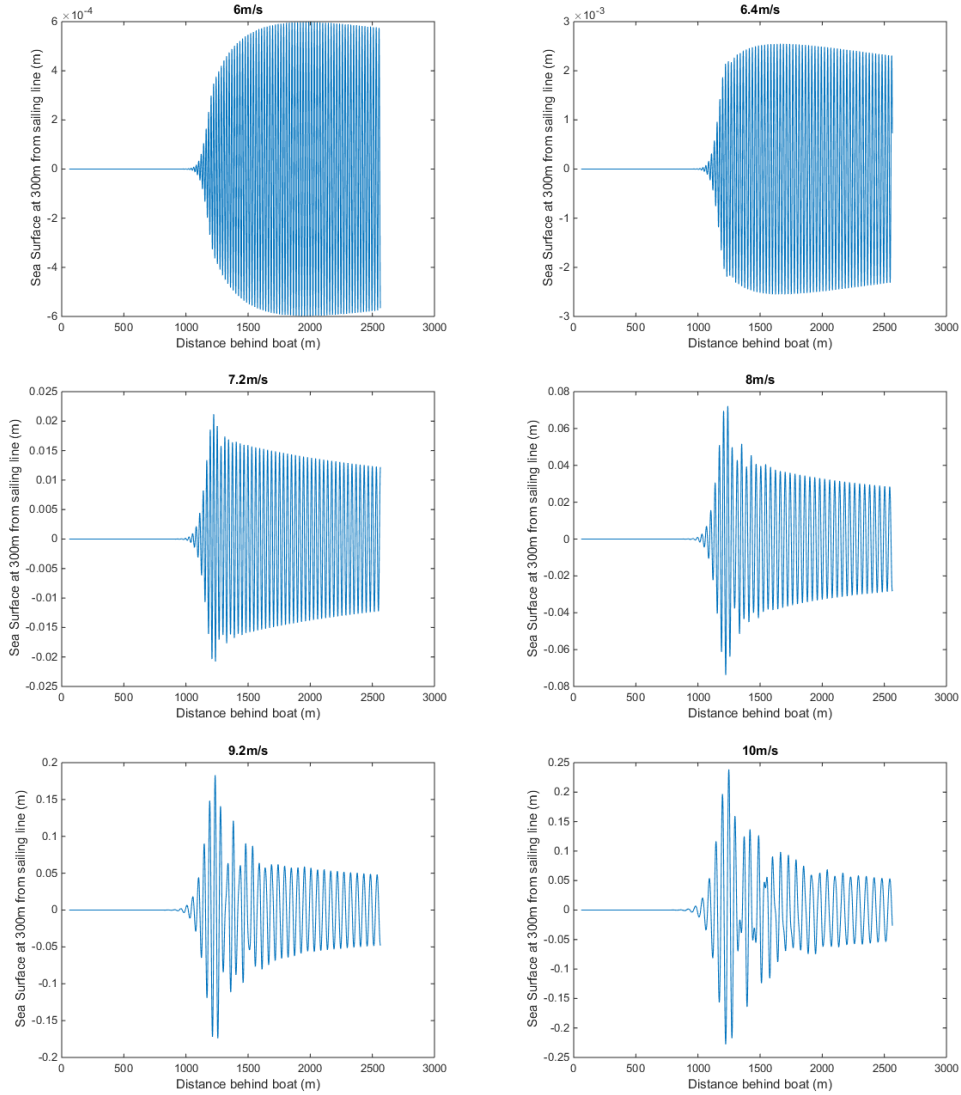


Figure 14: The sea surface at 300m from the sailing line at various Froude numbers. The boat velocities correspond to Froude numbers ranging from 0.2474 to 0.4124.  $b = 52\text{m}$ ,  $m = 3.36 \times 10^6\text{kg}$ ,  $W = 0.3$

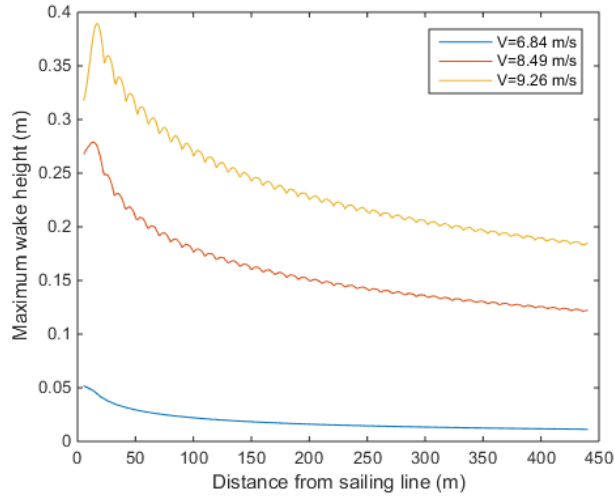


Figure 15: At greater distance  $D$  from the sailing line of the boat, the maximum wake height is smaller. Similarly, at lower boat speeds, the wake heights become smaller.

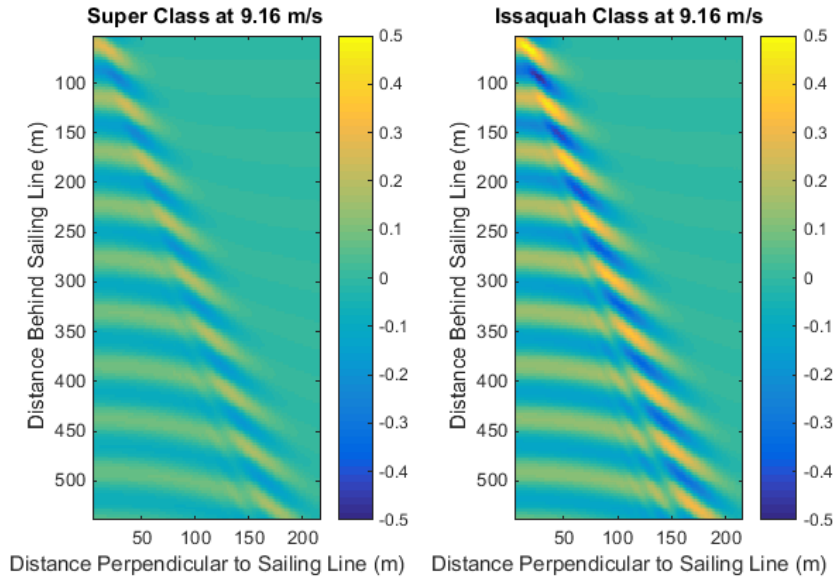


Figure 16: The Issaquah class vessel produces a wake roughly twice as large as the Super class when  $b$  is given by half of the linear vessel length,  $W$  is the vessel width to length, and the published vessel displacement figures are the masses.

boat is permitted to move, but its motion is constrained to vertical displacement and rotation about the width of the ship (heave and pitch). A wake structure from the reference frame of the ship develops in the time domain, and ultimately reaches an approximately steady state. So while technically unsteady, the model produces a wake structure that is effectively steady state.

### 3.2 Underlying Methods

The domain is governed by the Navier Stokes equations for incompressible, isothermal, and immiscible fluids, and the ship motion is calculated using rigid body dynamics. OpenFOAM refers to this solver as *interDyMFoam*. A flux limiter known as the multi-dimensional limiter for explicit solution (MULES) is employed to maintain a sharp air-water interface. Turbulence closure is achieved using the  $k - \omega$  equations. For further reference for these equations and their implementation, see [8].

The boundary conditions are as follows:

- The sides of the computational domain orthogonal to the direction of the bulk flow and the bottom are treated as symmetry planes
- The hull is treated as a no-slip barrier with no fluid flux and a zero normal gradient in pressure
- The inlet is given a uniform inlet velocity and hydrostatic pressure distribution
- The outlet pressure has zero gradient, and the outlet velocity is constrained to have the same mean velocity as at the inlet. This is enforced independently for both the air and water phases.
- The atmosphere is constrained to have zero total pressure and the velocity is a “pressureInletOutletVelocity” condition, which switches the velocity between a zero gradient condition and a fixed value determined from the normal flux, depending on the sign of the velocity.

### 3.3 Model Limitations

Surface tension is ignored, and the effects of variable water depth are not included. The domain was designed to have a constant water depth that falls safely within the classification of deep water waves for the boat wakes. Similarly, surface tension is ignored because at the large scale of the problem being considered surface tension effects are negligible. Because the motion of the boat is constrained to pitch and heave, arbitrary boat motions (i.e., turning) are not permitted. Solutions are limited to simple forward boat motion.

### 3.3.1 Vessel Mass

The model proved to be quite sensitive to vessel mass. Small increases in mass cause the vessel to submerge entirely. The fully laden vessel mass was unable to be achieved while accounting for rigid body dynamics of the vessel. As a surrogate, vessel heave could be fixed at a depth representative of the proper mass and the model run using the solver *interFoam*, which is similar to *interDyMFoam*, except rigid body dynamics are ignored and the mesh is not adaptive.

### 3.3.2 Scalability

Obtaining a higher resolution or larger domain solution scales fairly poorly in terms of computational complexity. If we wish to obtain sea surface values at a normal distance  $d$  out from the boat's position, the required mesh cells,  $n$ , scales as  $n \propto 3d^2$ , where the constant factor arises from the Kelvin Angle. OpenFOAM supports locally and distributed parallelism; parallel runs utilizing 8 cores on 16 GB RAM Ubuntu machine have been successful. Attempts to implement the model on a cluster computer capable of running on several hundred cores have on going technical challenges.

### 3.3.3 Numerical Dissipation

The numerical methods used by OpenFOAM introduce an artificial viscosity term to the Navier Stokes equations. This term is typically minimized, but is often required to maintain numerical stability during computations. In low-resolution mesh cells, this term dissipates significant amounts of wake energy, leading to an unrealistic decay of the boat wake. Repeated iterations over various mesh cell sizes have identified a maximum effective mesh cell size for which further mesh refinement does not alter the model output, but achieving this mesh cell size incurs high computational cost. Mesh refinement is performed using the *refineMesh* command in OpenFOAM. This command splits each 3-dimensional mesh cell in half along each dimension, resulting in eight new cells of equal size.

Fig. 17 illustrates the effects of numerical dissipation encountered in the OpenFOAM model and how it relates to mesh density. A critical change in the shape of the wake height decay occurs at the boundary where mesh resolution changes, at around  $d = 500m$  on the x-axis in the figure. The results beyond this critical point are deemed unreliable and unrealistic.

### 3.3.4 Interface Dilution

As with most multiphase Navier Stokes models, the interface between the different phases tends to "blur" over long time domain simulations. The MULES flux limiter does a decent job of maintaining a sharp interface, but, especially in low-resolution mesh situations, the interface loses some resolution. A consequence of this is that

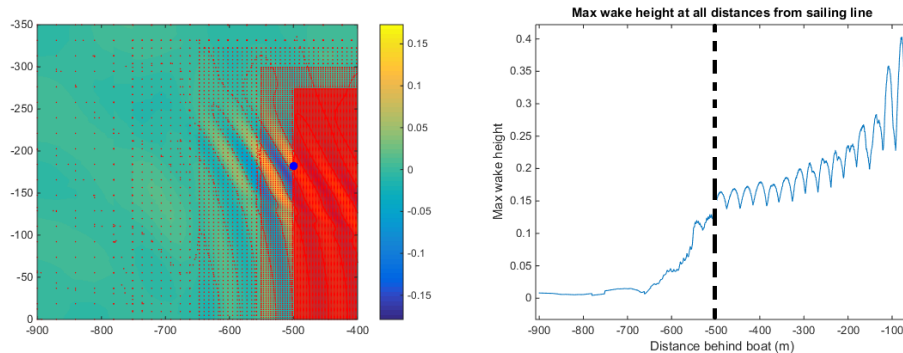


Figure 17: Left: A sea surface plot, overlaid with the centers of mesh cells. The underlying coloration represents the sea surface. The vessel would be located to the right of the plot, and be moving to the right. Right: plot of the maximum wake height as a function of distance behind the boat. The dashed line at 500m corresponds to the change in mesh resolution (denoted by the blue dot in the left figure.) After this critical point, the wake decays much more rapidly than we would normally expect.

the field variables at the exact surface are somewhat unreliable. Fig. 18 explores interface dilution visually. The interface between air (blue) and water (red) has spread to be two mesh cells wide. For our purposes, this is not considered to be a particularly negative result, as the vertical spacing of the mesh near the free surface ranges from 25cm to 2mm, across all mesh resolutions. For the regions determined to have good resolution in Section 3.3.3, the upper bound vertical mesh spacing was 15.6mm, or four iterations of mesh refinement where the cell sized is halved.

### 3.3.5 Turbulence Model and Boundary Layer Effects

The scale of the model prohibits the turbulent boundary layer from being well-resolved. The turbulence model used, the Smagorinsky scheme, is also known to be overly dissipative. When the turbulence is turned off, as in Fig. 19, the computational solution differs, but the decay of the wake as it moves out from the boat is qualitatively unaffected. It is unknown how the turbulence model affects the viscous drag on the boat model, since we are unable to fully resolve that scale.

## 3.4 Model Results

### 3.4.1 Transverse Wake

We can quantify the transverse wakes of the numerical model using the wavelength of wakes in the model output. Transverse wakes propagate at the ship velocity  $U$ , and so using the deep water phase speed relation  $c_p = \sqrt{\frac{g}{k}}$ , we arrive at an

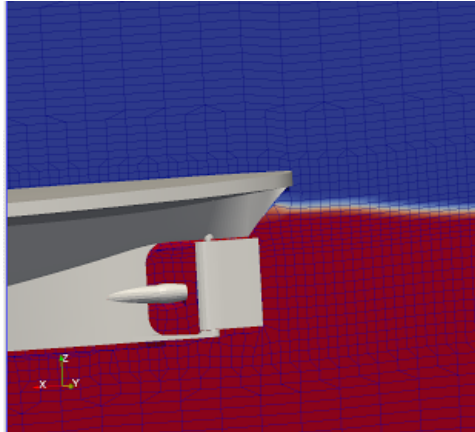


Figure 18: A zoomed in section of the computational domain, colored by average density of mesh cell. The mesh and the edge of a CAD model of the ferry are visible

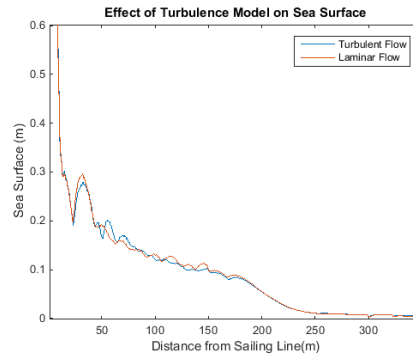


Figure 19: The OpenFOAM profile of the sea surface vs distance from sailing line is mostly unaffected by using a laminar flow model

expression that relates the velocity and the transverse wavelength:

$$U = \sqrt{\frac{g\lambda_t}{2\pi}} \quad (12)$$

For each of the Issaquah models, the positions of the crests of the transverse wake were measured from the simulation results and an implied velocity was calculated, according to Eq. (12). The results found that the transverse wake is best reproduced at higher velocities, but in all cases, it appears to be biased high, as seen in Table 1. The accuracy, however, was quite good overall. The Super class model also yielded good transverse wavelength agreement.

Vessel Speed (m/s)	$\lambda_t$ (m)	Implied Velocity (m/s)	Std. Err
Issaquah Class			
6.84	31.375	6.995	0.036
8.49	46.722	8.527	0.031
9.26	55.375	9.294	0.038
Super Class			
8.49	46.29	8.50	0.048

Table 1: Transverse wavelength and vessel speed data for Issaquah class modeled in Open-FOAM

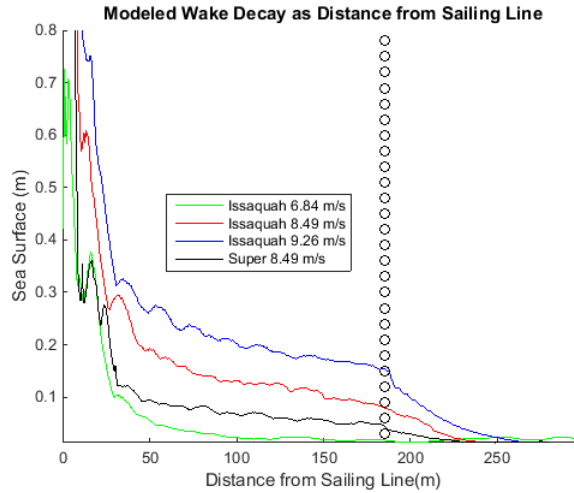


Figure 20: Maximum wake height versus distance from sailing line for several models. The dots indicate a change in mesh resolution that artificially steepens the rate of decay

### 3.4.2 Wake Height and Dissipation

A key component of the first objective specified in 1.2 is to understand how wake height falls off as the wake propagates farther from the ship. As shown in Fig. 17, the mesh resolution partially dictates this rate of decay, but it is nonphysical. Before the threshold where the numerical dissipation dominates, we can examine the maximum wake height as a function of distance from the sailing line and analyze that decay. Fig. 20 captures the decay. It is immediately clear that, as the analytic model in Section 2.5 indicates, the superclass produces a much lower wake at the same speed of travel.

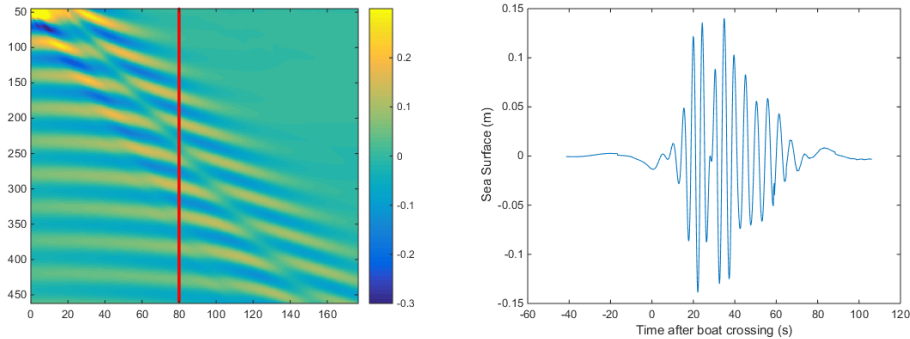


Figure 21: Left: A sea surface plot for an Issaquah at 16.5 knots, generated by OpenFOAM, overlaid with the relative trajectory of a theoretical wake buoy. Right: The time history of the wake that such a buoy would experience.

### 3.4.3 Sea Surface Time History

We may visualize a Lagrangian particle’s track by converting the stationary wake in the boat reference frame into the external reference frame. We define the transform

$$\zeta(x, y) \rightarrow \zeta(t, y)$$

via the relationship  $x(t) = Ut$ . In this form, we obtain a time domain measurement of the sea surface as if there were a numerical wave buoy in the simulation. This permits comparisons with reconstructed sea surfaces from the wave buoys. Fig. 21 illustrates this process. A transect is taken from a generic simulation result and converted to a time domain sea surface.

### 3.4.4 Sea Surface Velocity

A final useful metric from OpenFOAM data is the sea surface velocity. If we wish to compare the OpenFOAM model to field data, we may either transform raw field velocities into a sea surface estimate (see Section 4.2 below), or calculate surface velocities from the OpenFOAM data and compare directly to the raw field velocities. As discussed in 3.3.4, this method has some potential pitfalls. However, by taking the field values for velocity several grid points below the air-water interface, we can mitigate the effects of interface dilution while only introducing a nominal error of  $e^{-kz}$ , where  $k$  is the wavenumber and  $z$  is the distance below the sea surface. For small values of  $kz$  (long wavelengths and small distances below the surface) the correction is approximated by

$$u_{\text{true}} = u_{\text{meas}}(1 + kz).$$

Indeed, the wavenumbers and vertical grid spacing for this application introduce a theoretical error of less than 5%. Fig. 22 displays velocity data, both at the

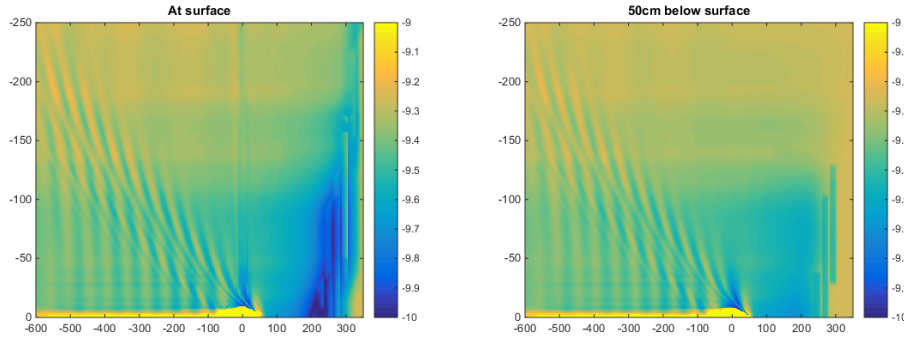


Figure 22: Left: A sea surface velocity plot for an Superclass ferry at 16.5 knots, generated by OpenFOAM. Right: the same velocity point, interpolated for the surface defined by 50cm below the sea surface. This distance spans at least three grid points.

surface and several grid points below the surface. In several locations, artificially high velocity gradients are smoothed out by taking values from subsurface cells, while the underlying velocity is not appreciably affected.

## 4 Time Domain Analysis

### 4.1 Field Measurements

On 17 September 2014 and 18 November 2014, the wakes of the ferry boats servicing the Seattle-Bremerton route were measured via data boys deployed from R/V Jack Robertson. An approximate sailing line for an approaching ferry was obtained from Automatic Identification System (AIS) vessel tracking data. Buoys were then deployed in a line running approximately perpendicular to the predicted sailing line of the ferry. The ferry crossing time was recorded as the time when the ferry intersected the array of buoys.

### 4.2 Buoy Analysis Methods

The SWIFT and  $\mu$ SWIFT buoys collected GPS position and velocity at a sampling rate ranging from 4 Hz to 10 Hz, depending on the exact device, via GPS logger (QStarz BT-Q1000eX). The horizontal positional accuracy of this, and most commercial GPS devices, is on the order of 10m. However, the relative horizontal velocity resolution is approximately 0.05 m/s through Doppler phase processing of the raw signals [7, 14]. The vertical elevation and velocity do not have sufficient accuracy to be considered for data processing. Therefore, the positional GPS data are used to obtain approximate locations and trajectories of the buoys, and the horizontal velocity data are used to capture the motion of the sea surface. Some typical buoy trajectories are presented in Fig. 29. Under strong currents, buoys would drift at up

to  $1 \frac{m}{s}$ . The effects of current on buoy trajectory are further discussed in Section 3. In linear wave theory, the motion of Lagrangian particles influenced by sinusoidal wave motion is given by

$$v(t) = a\omega e^{kz} \cos \theta(t)$$

for wave amplitude  $a$ , angular frequency  $\omega$ , wavenumber  $k$ , and distance below the surface  $z$ . Similarly, the surface elevation is given by

$$\zeta(t) = a \cos \theta(t)$$

For a particle on the surface, the sea surface may be obtained from the velocity via the relation

$$\zeta(t) = \frac{v(t)}{\omega} \quad (13)$$

The goal of the time domain analysis is, therefore, to obtain accurate and well-behaved values for  $\omega$  and  $v(t)$  in order to reconstruct the sea surface. Here, well-behaved refers to avoiding low-frequency velocity drift and artificially small values of  $\omega$

#### 4.2.1 Composition of Dataset

The raw data are stored as vectors of time, latitude, longitude, velocity, and heading. The  $\mu$ SWIFT buoys record data constantly, while the SWIFT buoys record in burst of approximately 10 minutes, and then switch off for approximately 5 minutes to perform onboard processing. In total, the dataset covers 19 unique wake events. On several occasions, data are missing for a specific buoy or wake because the buoy was not deployed or the onboard processing was taking place during the wake event.

#### 4.2.2 Extraction of Wake Events

For each wake event and buoy, the velocity vectors were plotted from 3 minutes before the ferry crossing time until 15 minutes after the ferry crossing time. Wake events were selected visually from the plotted data. An example of this process is illustrated in Fig. 23. If the buoy was deployed, but no wake event was discernible, the event was not counted in the time domain analysis. Determining the “end” of the wake events was particularly subjective. The wake events were observed during the data taking to persist for up to 5 minutes, with slowly decaying structure. However, the bulk of the energy and the maximum wake heights are contained in the early components of the wake and are easily discernible.

#### 4.2.3 Filtering

Temporally and spatially varying currents produce very low to zero- frequency oscillations in the velocity vectors. A low pass filter with a time constant of 15s was applied to the raw velocity data to obtain current profiles. This was then subtracted out from the raw data to obtain filtered data.

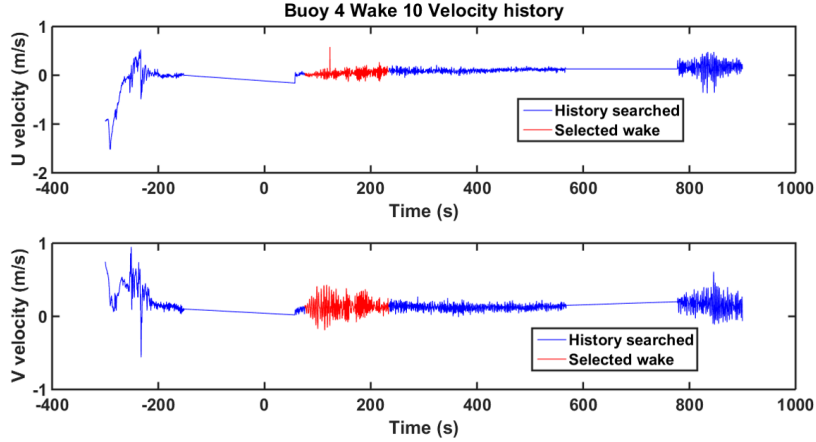


Figure 23: Searched velocity history for a SWIFT buoy and a generic wake event. The straight lines indicate periods where onboard processing prevented data from being collected. The two plots represent the orthogonal velocity vectors, and the red region highlights the active wake event.

#### 4.2.4 Diagonalization

A pitfall of the reconstructing the sea surface through linear wave theory is that a phase shift of  $\pi$  in a propagating wave is indistinguishable from a reversal in the direction of propagation. It is therefore impossible to perfectly reconstruct the sea surface from a linear combination of waves. In order to approximate the sea surface, the velocity vectors are transformed to correspond to the principal axes.

Fig. 24 illustrates the diagonalization process. For a best fit line forming an angle  $\theta$  with the compass direction axes, the velocity components for each data point are transformed using

$$\begin{pmatrix} \hat{u} \\ \hat{v} \end{pmatrix} = \begin{pmatrix} u \\ v \end{pmatrix} \begin{pmatrix} \cos \theta & -\sin \theta \\ \sin \theta & \cos \theta \end{pmatrix}.$$

The  $\hat{u}$  vector is then treated as containing the ship wake action. This method is most effective when the signal to noise ratio for the wake is large. However, in cases with a weak signal to noise ratio, because only one dimension of buoy motion is considered, the background noise is still reduced.

#### 4.2.5 Zero Crossing and Sea Surface

Due to the dispersion of water waves, the angular frequency  $\omega$  tends to increase throughout the duration of the wake. In order to use Eq. (13) to reconstruct an approximate sea surface, a time varying value for  $\omega$  must be obtained.

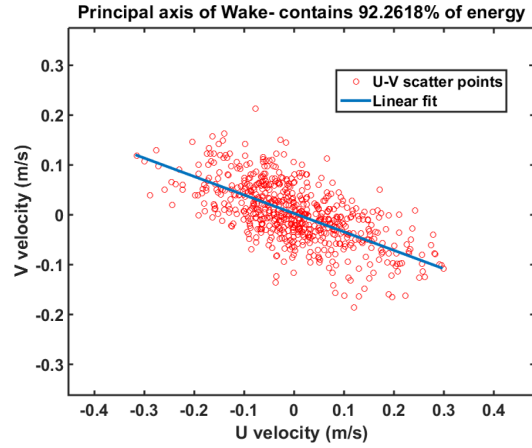


Figure 24: Scatter plot of velocity components at each data point during a wake event. A least squares linear regression best fit line determines the principal axis of the wave motion.

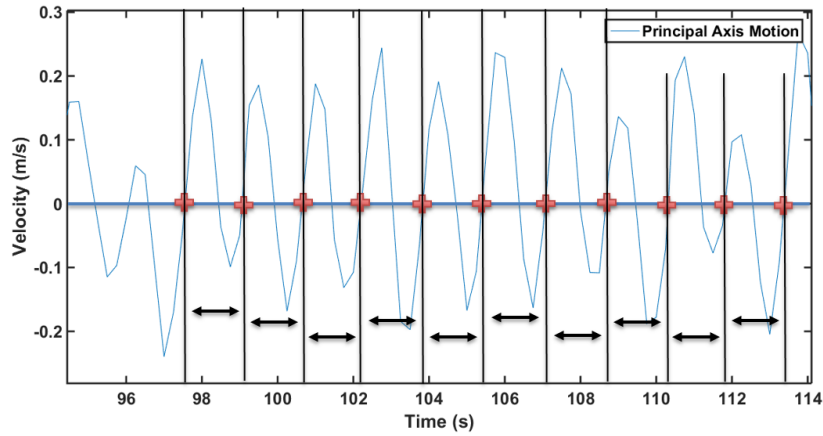


Figure 25: Illustration of zero crossing analysis. Every time the filtered and diagonalized velocity changes from negative to positive, a new wave period is measured. The time-varying angular frequency is determined from the periods

Values for  $\omega$  are calculated by measuring the period,  $T$ , between upward zero crossings in the velocity vector (Fig. 25).  $T(t)$  is then formed as a piecewise constant function in time, and

$$\omega(t) = \frac{2\pi}{T} \quad \rightarrow \quad \zeta(t) = \frac{v(t)T(t)}{2\pi}$$

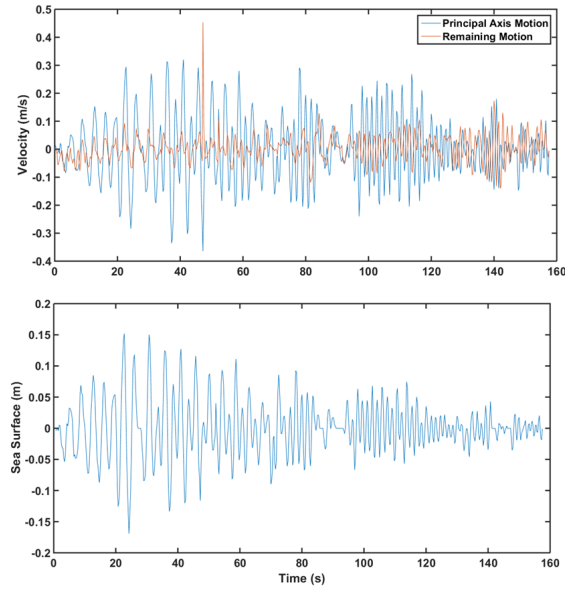


Figure 26: Comparison of sea surface and filtered, diagonalized velocity vectors.

Fig. 26 illustrates the transition from the diagonalized velocity time series to the sea surface time series. The minor axis wave motion is thrown away in this calculation. In this typical example, the wave series between  $t = [100, 120]$  is notably lower because while the velocity peaks are high, the angular frequency is also quite high. Around  $t = 140s$  the minor axis motion exceeds the principal axis motion, and this information is lost. Such an observation is common at the ends of the time series. It is believed the cause of this is that the direction of propagation of the wake changes slightly throughout the duration of the wake event. The tail end of the wake event is very low energy, and so the effects of this have been ignored.

## 4.2.6 Distance Calculation

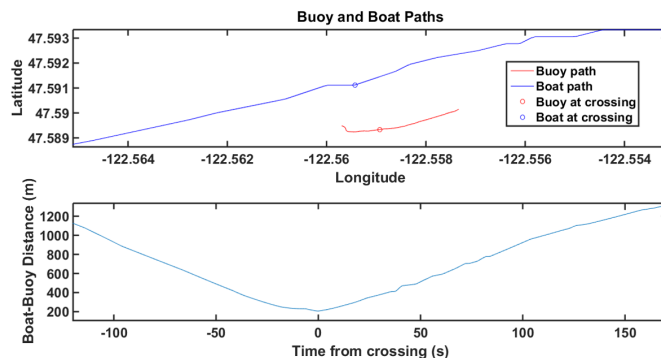


Figure 27: Illustration of the distance from sailing line metric

It is relevant to obtain a “distance from sailing line” metric for buoy measurements. We define distance from sailing line as the minimum distance between the ferry boat and the buoy as the ferry passes the buoy. Fig. 27 illustrates spatially how this metric is calculated. The above definition assumes spatially uniform ocean currents at the length scale of the buoy-boat separation. It is known that this assumption does not uniformly hold, but for most wake measurements, variations in the current tend to be small relative to the overall current, and primarily in the streamwise velocity along the ferry motion, which minimizes the effect.

## 4.3 Pressure Gauge Analysis

Two Aquadopp profilers were deployed in 24cm and 33cm of water during low tide on a gently sloping beach off of the property of resident Bill Cairn on 18 November 2015. Throughout the course of the day, the tide rose 1.77m. The AQD’s recorded static pressure, which allowed for the local sea surface to be calculated using the standard relationship for hydrostatic pressure with a water column of height  $h_{\text{water}}$ :

$$p_{\text{gauge}} = \rho g h_{\text{water}}.$$

The AQD’s were operating in the shallow to intermediate depth regime with respect to linear wave theory, so results are not readily comparable to buoy data. Rather, AQD data are used to assess the waves experienced at the shoreline.

### 4.3.1 Results

All of the Aquadopp-recorded wake events exhibited some form of packeting, where the peak amplitude oscillated in time. The Superclass vessels also all exhibited a low frequency forerunner wave, as shown in the top image of Fig. 28. Such waves were not observed for the Issaquah class vessels, and appeared for the Superclass,

regardless of vessel and current direction. There is no proposed mechanism for this observation, currently.

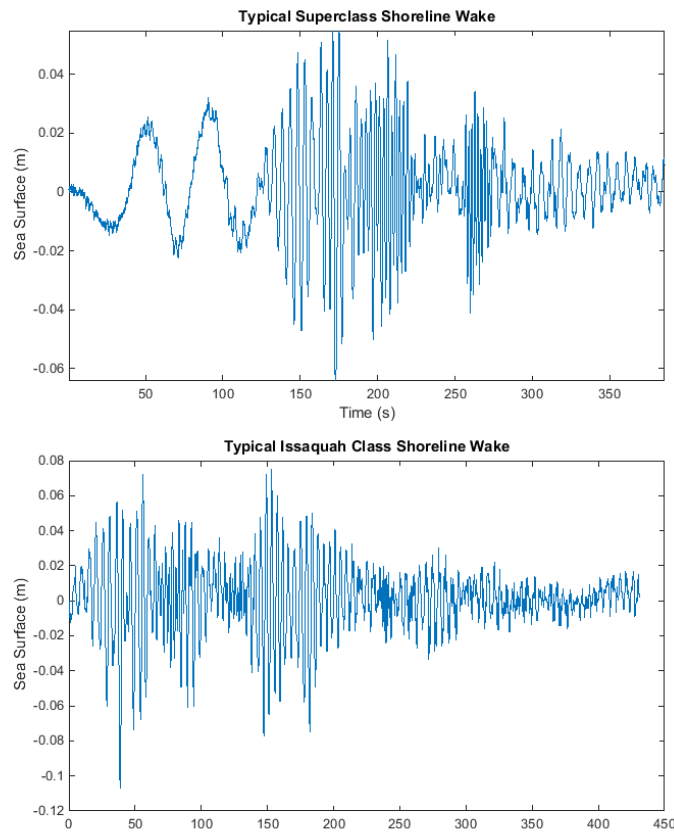


Figure 28: Typical processed sea surface plots for AQD pressure sensors

#### 4.4 Validation

The buoy data were checked for consistency in order to identify problematic measurements that should be excluded from wake calculations.

#### 4.4.1 Cross-Buoy Comparison

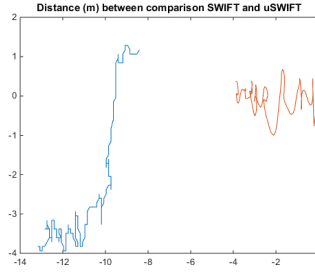


Figure 29: Relative GPS tracks of the selected SWIFT and  $\mu$ SWIFT buoys. Axes are relative distances, in meters. The buoys were located within margin of error of the GPS devices (14.1m, when taken in quadrature) relative to each other for the duration of this wake event

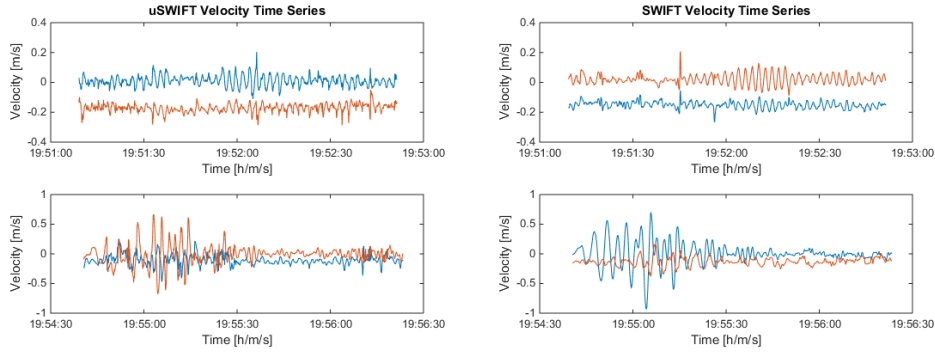


Figure 30:  $\mu$ SWIFT and SWIFT raw time series data for background and wake. The two lines per plot indicate the orthogonal velocity components.

For one wake event, a  $\mu$ SWIFT and a SWIFT buoy were placed within 10m of each other in order to compare buoy performance. The Lagrangian buoy tracks are shown in Fig. 29 and the raw velocity data is shown in Fig. 30. The buoys have good qualitative agreement in terms of timing and shape of the plots. In general, the SWIFT buoy produces higher quality data – it is two orders of magnitude more expensive and has a longer track record of successful deployments.

#### 4.4.2 Group Velocity Propagation

If the wake generation of a ferry boat is assumed to be a Dirac delta function, this is represented as a broadband pulse in the frequency domain. Waves of all frequencies are generated simultaneously and add linearly. Then, the dispersion relation for gravity waves governs the propagation velocity for each frequency. For a Dirac

pulse at time  $t = 0$  and location  $x = 0$ , with a dispersion relation<sup>2</sup>  $\omega(k) = \sqrt{gk}$  the observed frequency  $\omega(x, t)$  is given by

$$\omega(x, t) = \frac{gt}{2x} \quad (14)$$

This expression comes from a rearrangement of the simple kinematic expression  $x(t) = tv(t)$ . Note that in Eq. (14) the expression for velocity is the group velocity,  $\frac{g}{2\omega}$ , rather than the phase velocity. Now, for constant  $x = d$  (i.e. a stationary buoy in the reference frame of the still ocean surface under the influence of current) the observed frequency should increase linearly in time with slope  $\frac{g}{2d}$ .

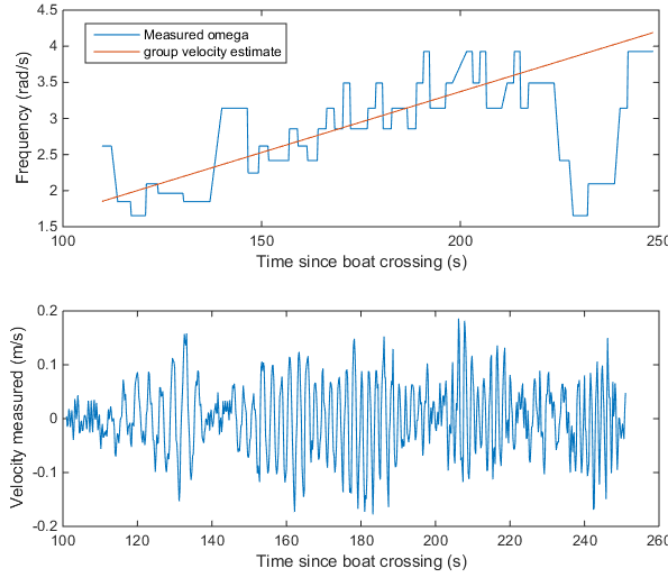


Figure 31: Comparison of predicted  $\omega$  via Eq. (14) and observed  $\omega$  tabulated in the method detailed by Fig. 25

We indeed observe, Fig. 31 being a typical case, that the group velocity is a good predictor for the angular frequencies observed by the buoys. This is a useful check in cases where the distance from sailing line is difficult to determine.

## 4.5 Results

The most useful metric to be obtained from sea surface reconstruction is the maximum wake height. Again, we create plots of the distance from the sailing line and

<sup>2</sup>This is the deep water limit, typically invoked when the water depth is greater than half of the wavelength. The water depth in Rich Passage (see section 9.1) permits this deep water limit for wavelengths less than approximately 40 meters (corresponding to periods up to 5s)

maximum wake height, for various vessel designs and speeds. The Superclass did not slow down in Rich Passage- maintaining  $17 \pm 1$  kts in both Port Orchard and Rich Passage. The Issaquah also maintained  $17 \pm 1$  kts outside Rich Passage, but slowed down to  $12 \pm 1.5$  kts in Rich Passage, as per WSF’s agreement. We see in Fig. 32 that the Superclass wake is significantly lower.

#### 4.5.1 Wake Height Plots

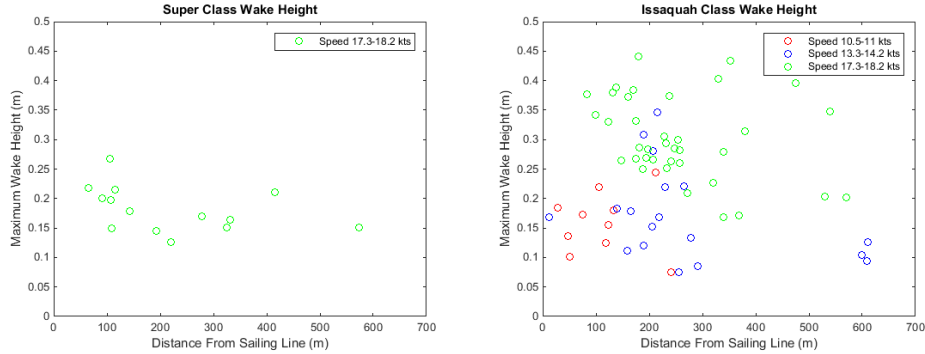


Figure 32: Comparison of maximum wake heights. The greatest wakes are produced by the Issaquah class vessels moving at high speed.

#### 4.5.2 Boat Velocity Conclusions

The slowdown produces a significant reduction in wake height for the Issaquah class. The Superclass data are more sparse, because it ran fewer transits during data collection. However, the data displayed in Fig. 32 demonstrate that the full-speed Superclass produces much smaller peak wake height than the full-speed Issaquah, and qualitatively comparable wake heights to the speed-limited Issaquah class. The field data support the conclusions obtained in [9] and shown in Fig. 2.

### 5 Frequency Domain Analysis

A frequency domain analysis of the field data provides additional information about the background sea state and wake signals.

#### 5.1 Methods

The spectral density function (SDF) is calculated using the periodogram [11]. A lag window estimator is also used where noted. All results are based on 1024-point time series obtained from the field work discussed in Section 1.5. Use of the periodogram is typically ill-advised as a spectral estimator, but for the spectra encountered and the frequencies of interest, it yields nearly identical results to ”unbiased” methods

that require data to be thrown away. Because the periodogram has good accuracy while preserving data, it is used for this application. The specific mathematical methods are discussed in greater detail in Section 9.4.

## 5.2 Background Spectral Analysis

The background spectra describe the ambient conditions that the buoys are experiencing in the absence of boat wakes. This serves to provide information about the sea state as well as the response functions of the buoys. By comparing the signal spectra to the background spectra, we might better identify frequencies that are present in the wakes vs merely excited by buoy resonance. A dataset of background sea motion was obtained by choosing 1024-point series that did not have significant wave action. A typical series may have occasional large movements, and a drift velocity, but the sea state will be relatively constant. However, the sea state may be very different between series.

### 5.2.1 SWIFT Background Spectra

The SWIFT buoys are identical in their construction and operation. Therefore, we expect that the spatial and temporal sea state should be the only factor affecting buoy spectra. To check this assertion, time series from when the SWIFT buoys were aboard the main vessel were analyzed. The resulting spectra represent the boat's response to the sea state throughout the date.

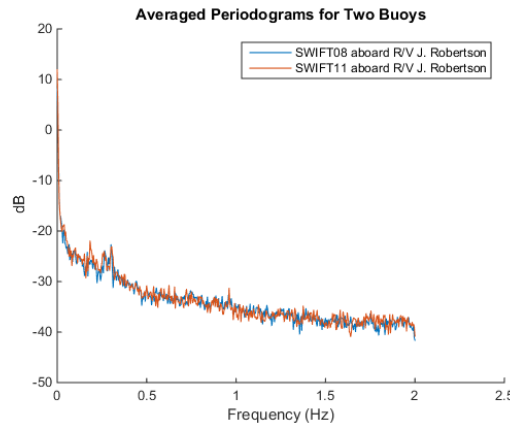


*Figure 33: A comparison of time series obtained from SWIFT buoys aboard the main vessel. The expectation that the SDF functions should be equivalent is confirmed.*

As expected, the spectra displayed in Fig. 33 are very close together. Note that due to limitations of the internal processing of the buoys, the exact time series used were taken at slightly different times between the buoys, so very small variations are expected.

The same procedure was performed for two SWIFT buoys deployed in different locations off of Port Orchard in Puget Sound. Periodograms obtained from time series over the course of 90 minutes were aggregated to obtain a combined SDF estimate for each buoy.

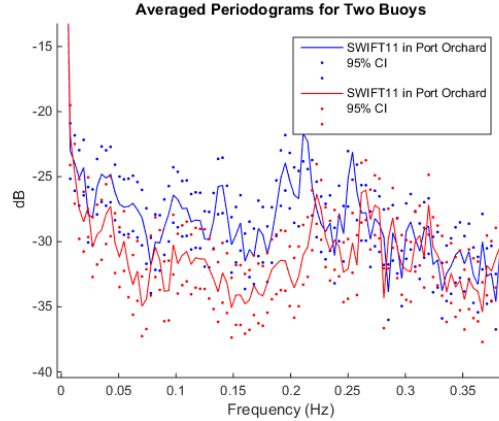


Figure 34: Spatial variation in background sea state is observed between two locations separated by approximately 1km

While the SDF estimates shown in Fig. 34 have very similar shapes, the signal level differs by a statistically significant amount, and the locations of the peaks appear slightly different. While this spatial variation in spectra might initially seem large, we can also compare data from the Rich Passage, Port Orchard, and control (aboard the research vessel) locations in Fig. 35.

Above about 0.4 Hz, the Jack Robertson buoys exhibit a very stable rolloff, while the deployment locations have a series of distinct and different peaks up until 0.9 Hz. We can conclude that the peaks between 0.4 and 0.9 Hz are due to buoy-water interaction that is not captured by the motion of the search vessel through the water. Compared to Figure 34, the variation in SDF is much greater between Rich Passage and Port Orchard than for variation within each general location.

### 5.2.2 $\mu$ SWIFT Background Spectra

The  $\mu$ SWIFT background spectra proved to be highly varied, with few broad trends. Whereas the SWIFT buoys seemed to be sensitive to the deployment location, the  $\mu$ SWIFTs seemed to be sensitive to the specific deployment.  $\mu$ SWIFT04 is analyzed in Fig. 36 for 4 separate deployments, with several background spectra taken for each deployment.

Deployments 1 and 4 had a much higher noise floor than deployments 2 and 3, despite deployments 1 and 2 being in Port Orchard and deployments 3 and 4 being in Rich Passage. This effect, however, was not constant across all of the  $\mu$ SWIFTs.

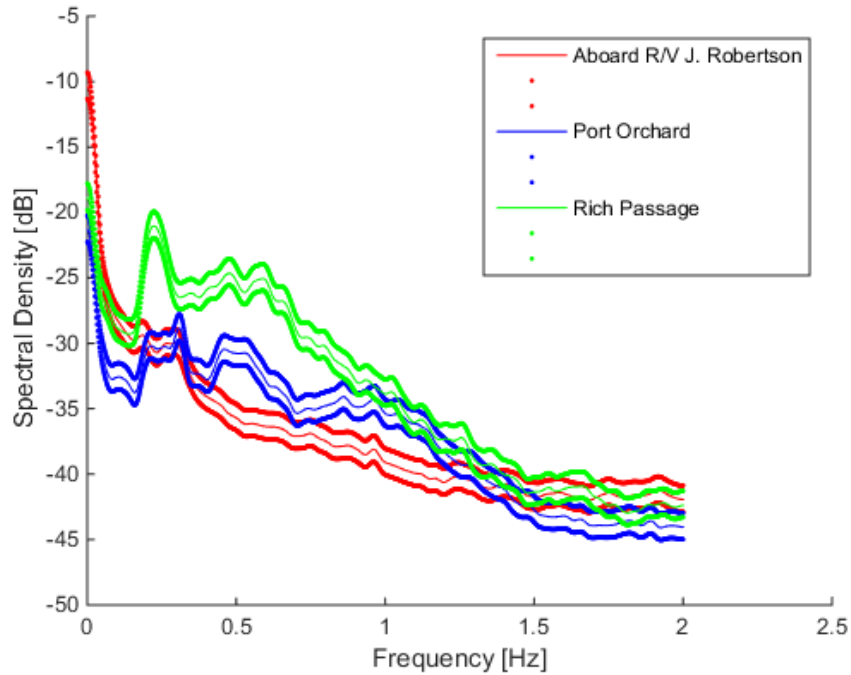


Figure 35: Aggregated Gaussian lag window with  $m=20$  estimates for the various buoy locations

When the wake signals are analyzed, the spectra for each of the 4 deployments seem to adopt the higher noise floor that is seen in the background spectra for deployments 1 and 4. This is illustrated by Fig. 37, where four background signals (red and blue) and the four wake signals immediately following them (black) are plotted.

### 5.3 Side by Side Buoy Comparison: A Case Study

On the November 18 data taking day, a  $\mu$ SWIFT buoy and a SWIFT buoy were placed next to each other during a wake event, for the purpose of comparing the quality of the recorded data between the two types of buoys. The raw data are summarized in Fig. 38.

#### 5.3.1 Background Signal Spectral Estimates

As before, the dynamic range in the frequency domain is small enough that the periodogram is unbiased. This is readily confirmed with a prewhitened/postcolored spectral density estimate. The periodograms show what appears to be a peak on the order of 0.07 Hz in width. To generate a lag window estimate that captures this,

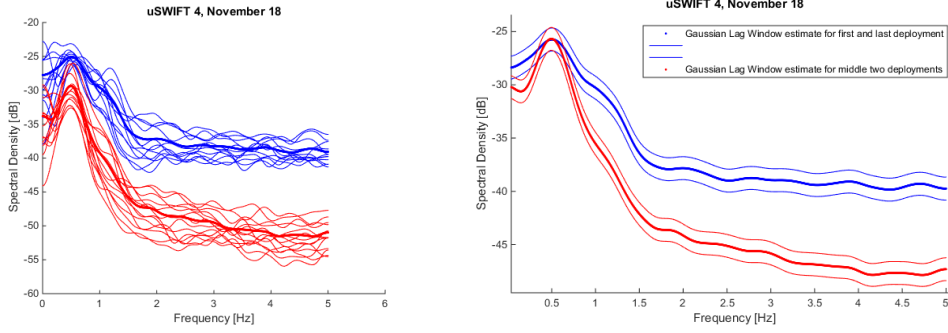


Figure 36: Background spectra for  $\mu$ SWIFT04. The left image shows the Gaussian Lag ( $m=30$ ) SDF for each time series, and the right image is the combined SDF with 97.5% confidence interval.

we choose a  $B_W$  of 0.05Hz, and then solve

$$B_W = \frac{1}{\Delta t \sum_{\tau=1}^{N-1} w_{m,\tau}} [11]$$

for the correct choice  $m$ , yielding  $m = 174$  (see Section 9.4). This choice of  $m$  for this lag window gives good smoothing while preserving the apparent features in the spectral density functions. The equivalent degrees of freedom for the periodogram estimates are 4 each, and 9.66 for the lag window estimates. The latter corresponds to approximately a 2.59 dB band, forming the 97.5% confidence interval.

The background spectra are plotted in Fig. 38. It is notable that below 1.8Hz, the spectra track each other quite well, but above this value, the SWIFT buoy has a noise floor that is nearly 20 dB lower, and also two fairly substantial peaks that are not seen in the uSWIFT spectrum. However, because these peaks are still below the noise floor in the uSWIFT spectrum, we cannot verify whether or not they would be present.

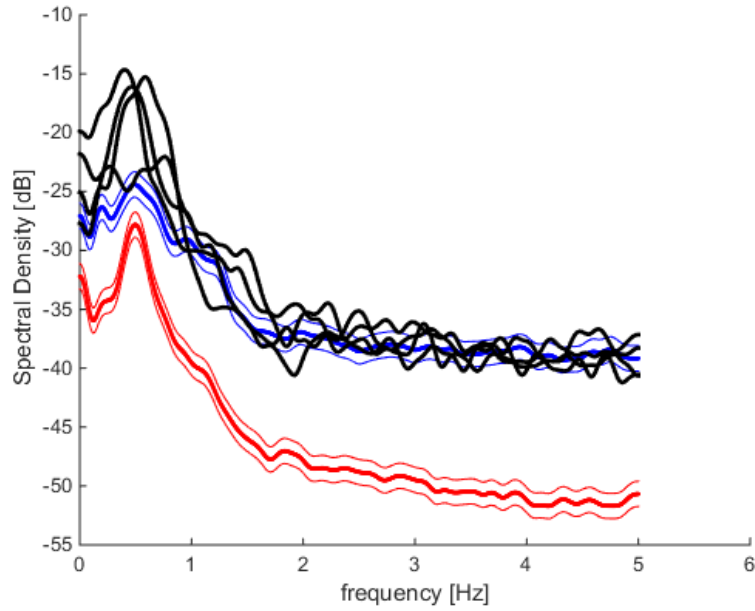


Figure 37: Black SDF spectra are the  $m=40$  Gauss Lag SDF Estimates for the wake signals

### 5.3.2 Wake Signal Spectral Estimates

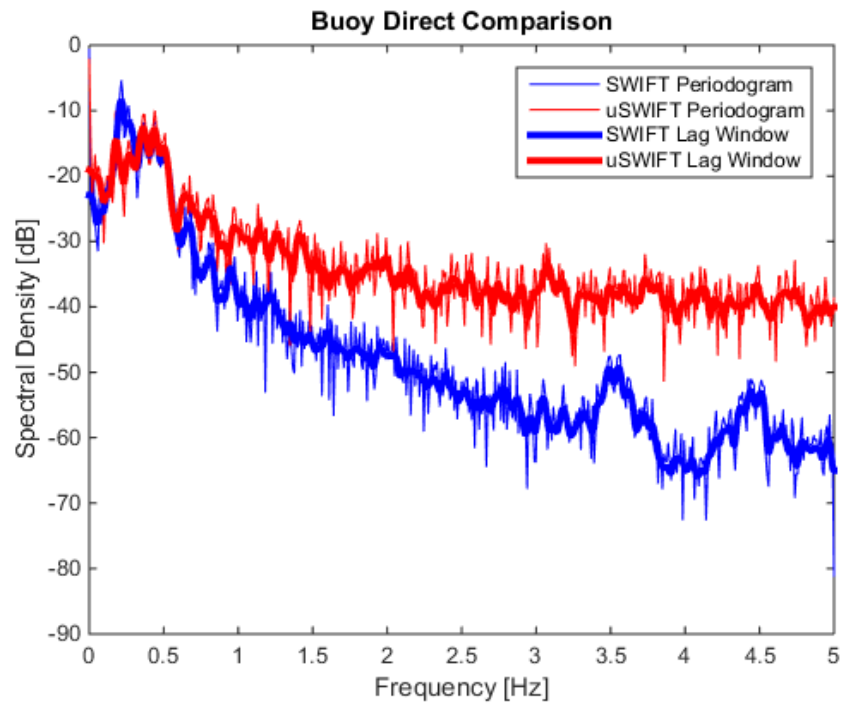


Figure 40: Wake signal spectra

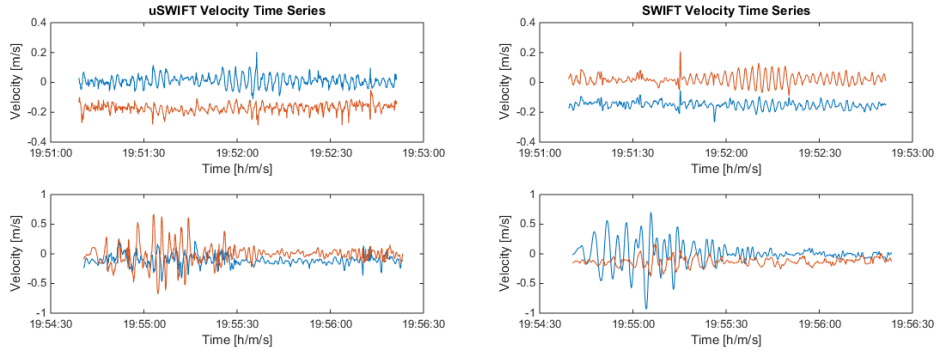


Figure 38:  $\mu$ SWIFT and SWIFT raw time series data for background and wake. The two lines per plot indicate the orthogonal components

Once again, the SWIFT buoy has a much lower noise floor, and presents two peaks around 3.5 and 4.5 Hz. In this instance, the peak widths are greater, but the locations are unchanged, and once again, the uSWIFT does not pick these up. Whereas the frequencies of these peaks are much greater than the frequencies of interest (roughly 0.1 to 1 Hz), we dismiss them as interesting artifacts of the sea state, but ultimately unrelated to the wake analysis.

To obtain a better intuition, we can look at the individually-smoothed orthogonal velocity spectra (see Fig. 41).

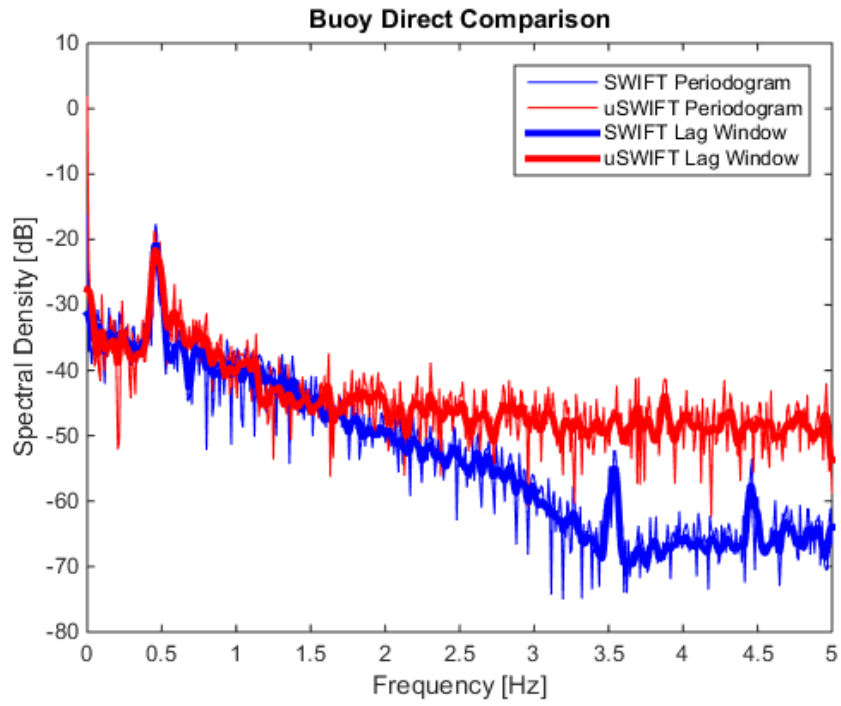


Figure 39: Background signal spectra

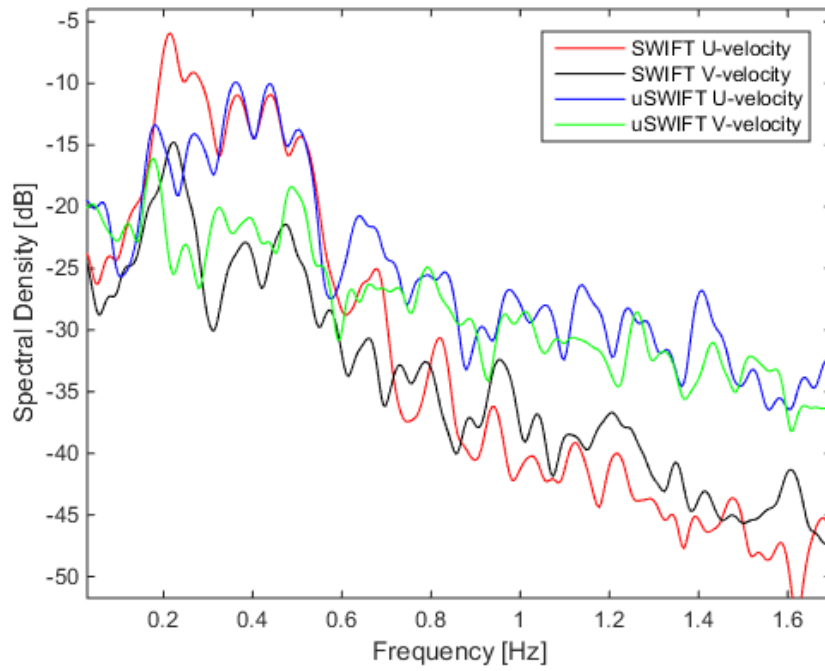


Figure 41: The orthogonal velocity component spectra for each buoy during the wake event

At frequencies lower than 0.55 Hz, the U-components and V-components of each buoy track each other fairly well. The notable exception is in the range 0.16 to 0.27 Hz, where they behave significantly differently, as is also observed in Figure 40. This discrepancy appears to be due to the buoys themselves. Above the 0.55 Hz threshold, the spectra for the U-V components approach each other, while diverging between buoys. The frequency range [0.33, 0.57]Hz is the range of best agreement between the two spectra- well-within the uncertainty for these estimates.

### 5.3.3 Cross Spectra

Because the buoys were only separated by approximately 10 meters, we can assume that they received the same signal, with a time lag. The cross covariance sequence was computed via

$$\hat{s}_{12,\tau}^{(p)} = \frac{1}{N} \sum_{\tau=1}^{N-\tau} X_{1,t} X_{2,t+\tau}$$

and the maximum value was determined to occur at a lag time of 0.2 s, or  $2\Delta_t$ , as shown in Fig. 42.

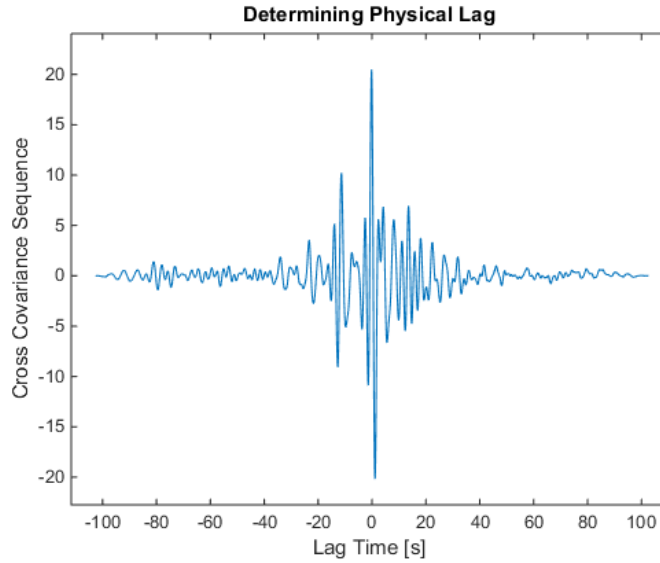


Figure 42: The maximum value of the CCS determines the physical lag between buoys. We find that the buoys are receiving nearly simultaneous signals

Unfortunately, due to limitations of the hardware, this implied physical lag is significantly smaller than the uncertainty due to the onboard data loggers on the buoys. We are incapable of synchronizing the buoys to within a few seconds of an absolute time. This method may prove fruitful when the known physical gap between buoys is larger. This is left as a future extension.

The Fourier transform of the cross covariance sequence yields the cross periodogram Fig. 43, which contains several interesting features.

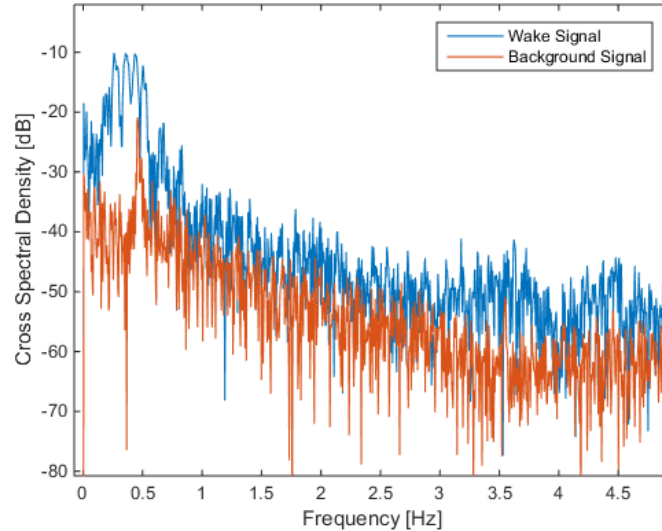


Figure 43: Several distinct peaks are observed in the signal cross periodogram, each with a width of approximately 0.05 Hz.

The effect of the signal is readily observable in the cross periodogram for the wake event. The background signal appears visually as though it might obliterate much of the observed wake signal, but due to the log scale, the wake signal is almost completely unaffected by subtracting out the background signal. Interestingly, the cross spectrum appears to have leveled the sporadic peaks from the individual buoy spectra into a series of peaks of similar height. This is highly reminiscent of the results seen in the AQD profiler, discussed below. A possible conclusion from this result is that each buoy individually captures part of the desired signal, and by performing a cross spectral analysis, we can recover a more accurate representation of the true signal.

The AQD profiler was located in approximately 2 meters of water on the shoreline and recorded a time history of the pressure, which scales linearly with the height of the waves above it. By taking the periodogram of the pressure time series for the same wake event as the direct comparison is measuring, we can attempt to compare the shape of the spectra, as shown in Fig. 44.

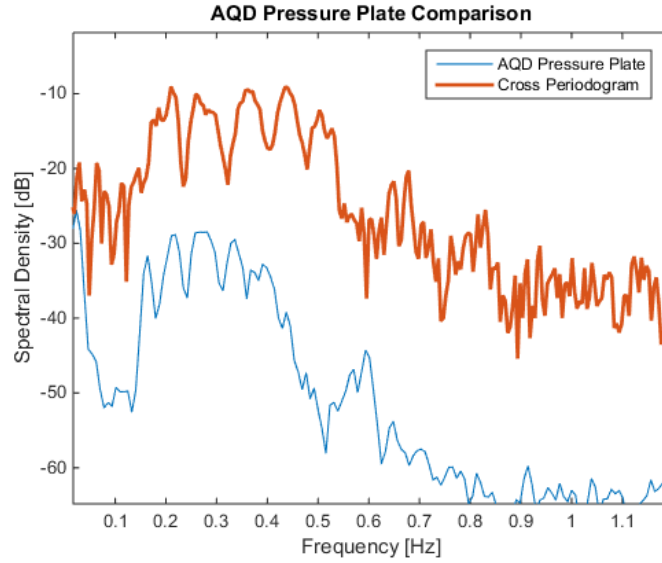


Figure 44: Comparison between the sum of the cross spectra  $S_U(f)$  and  $S_V(f)$  taken between the two buoys, and the periodogram of the AQD pressure time series

The five peaks are distinctly visible in both series, which suggests that this cross spectral technique may have some validity. The peaks are somewhat shifted between the two spectra. This is due to the dispersive nature of the medium. Lower frequency oscillations travel faster, and so a red shift is expected since the AQD profiler was located farther away. Some possible confounding factors in this conclusion are that shallow water effects may play a role, and the exact effect of dispersion on the spectral density functions has yet not been considered as of the writing of this paper.

#### 5.4 Maximum Wake Height Frequency

The angular frequency associated with the maximum wake amplitude (calculated via the zero crossing method outlined in Section 4.2.5) for a wake event was recorded. In general, the observed frequency was lower at larger distances from the sailing line, as the dispersion relation for deep water waves would suggest. However, the relationship between angular frequency and maximum wake height, Fig. 45, demonstrated a trend that appears to depend on the vessel speed. The most energetic waves are the ones with low angular frequency and large maximum height. Therefore, it is particularly concerning that the largest wakes associated with higher vessel speeds are also the lowest frequency wakes.

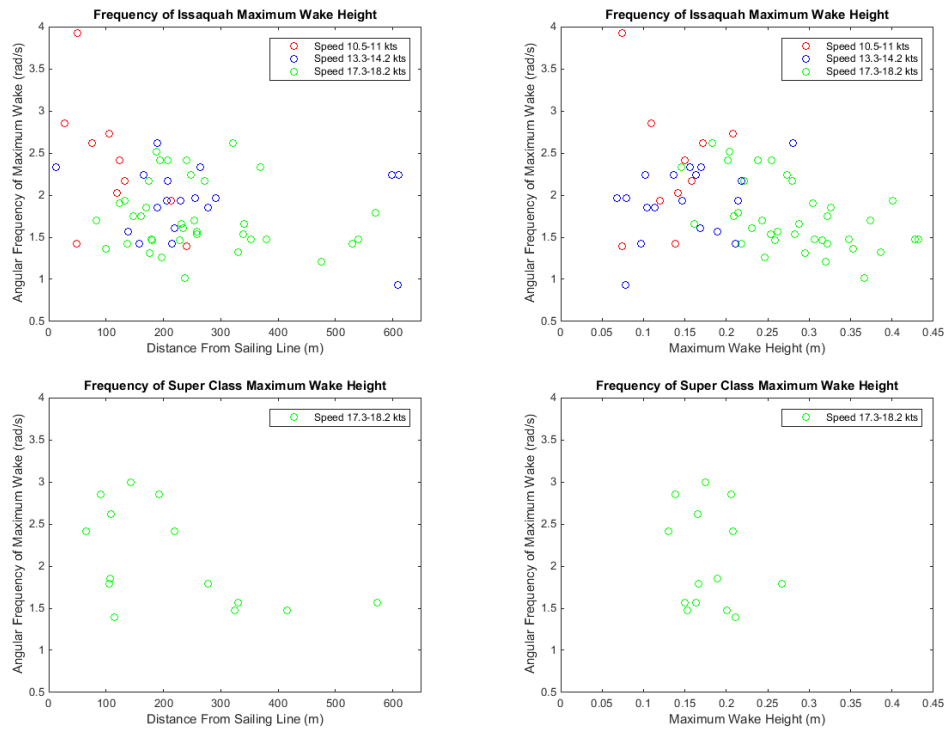


Figure 45: Angular frequency of the highest amplitude wave in the wake train is plotted against maximum wake height and distance from sailing line.

## 5.5 Frequency Domain Conclusions

The ambient spectra for the SWIFT buoys were found to be highly dependent on the deployment location of the buoy, and fairly consistent across the different buoys. Nonetheless, temporal and spatial variations dominate the magnitudes of the background spectra, while the basic shapes are somewhat more consistent. Applying a Gaussian Lag window in conjunction with combining lag window spectral estimates allows us to obtain much tighter confidence intervals than using simple direct spectral estimates. Prior knowledge about peak structure allows us to make full use of this procedure while avoiding the obliteration of physically significant peaks. Finally, the cross spectrum appears to be a promising avenue for analyzing the same wake event at different locations. In the only available direct SWIFT/ $\mu$ SWIFT comparison at close distance, the cross spectrum appeared to recover the wake packeting that was seen in a more reliable (but location-restricted) pressure sensor instrument. The dispersive nature of the gravity waves should be accounted for, however, when buoys with more separation are considered.

## 6 Model Comparison and Validation

In sections 2, 3, and 4, wakes were calculated using analytic, computational, and experimental methods. In this section, their results are compared in order to obtain a better understanding of the capabilities of the analytical and computational methods.

### 6.1 Wake Height Plots

Maximum sea surface versus distance from sailing line was compared across all sea surface metrics. The analytic models had the  $b$  and  $W$  parameters tuned to give a qualitative match to the data. These physical parameters, the length for calculating the Froude number, and the ratio of the elliptical axes of the pressure distribution do not directly correspond to the physical length and width of the vessel, and so were fitted within the parameter space of what they could possibly be physically. Fig. 46 displays the overall comparison between the various wake measurements studied. The analytic model does a good job of capturing the decay in wake height with distance that is observed in the field data. At high speed, the analytic model reliably reproduces the data observed. Both the analytic and the computational model are unable to capture the lowest regime of velocity accurately, however. The analytic model suffers a "Froude number panic" where the diverging wake disappears and the much smaller transverse wake dominates. This is expected to happen at some point, but it clearly happens earlier in the model than in the field data. In fact, the field data suggest that the diverging wake dominates at all times. The computational model appears to suffer from a similar Froude panic, but this is also compounded by numerical errors associated with the meshing. The OpenFOAM model consistently

underestimates the wake, and also overestimates the rate of decay with distance from the sailing line. This points to numerical dissipation, as well as the mass of the vessel not being accurately represented in the calculation.

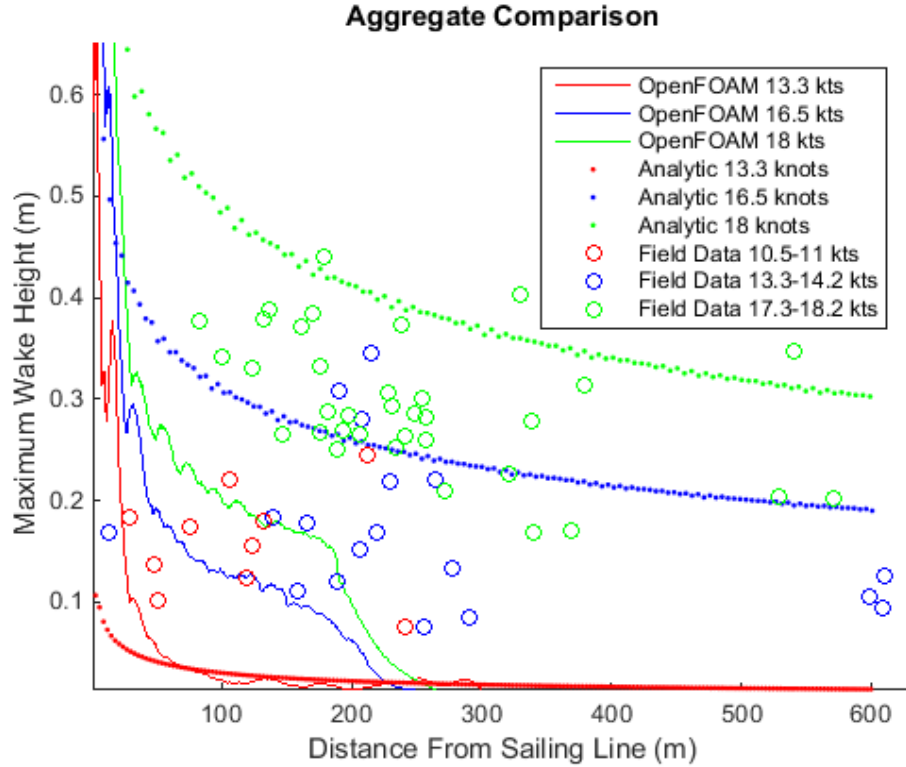


Figure 46: Comparison of maximum wake heights for an Issaquah class vessel, across the various models.

## 6.2 Lagrangian Tracking Comparisons

Several direct comparison were made using the Lagrangian tracking method outlined in section 3.4.3, and are shown in Fig. 21. For additional plots, see Section 9.3. This method is quite sensitive to clock synchronization between the vessel and buoy, as well as vessel speed. Several representative comparisons are presented below, chosen from the cases where the data buoy produced good data and was located in a physical region and vessel speed where OpenFOAM results were available. OpenFOAM tends to underestimate the sea surface, but frequently includes wake structure that matches the buoy measurements, but is not present in the analytical model.

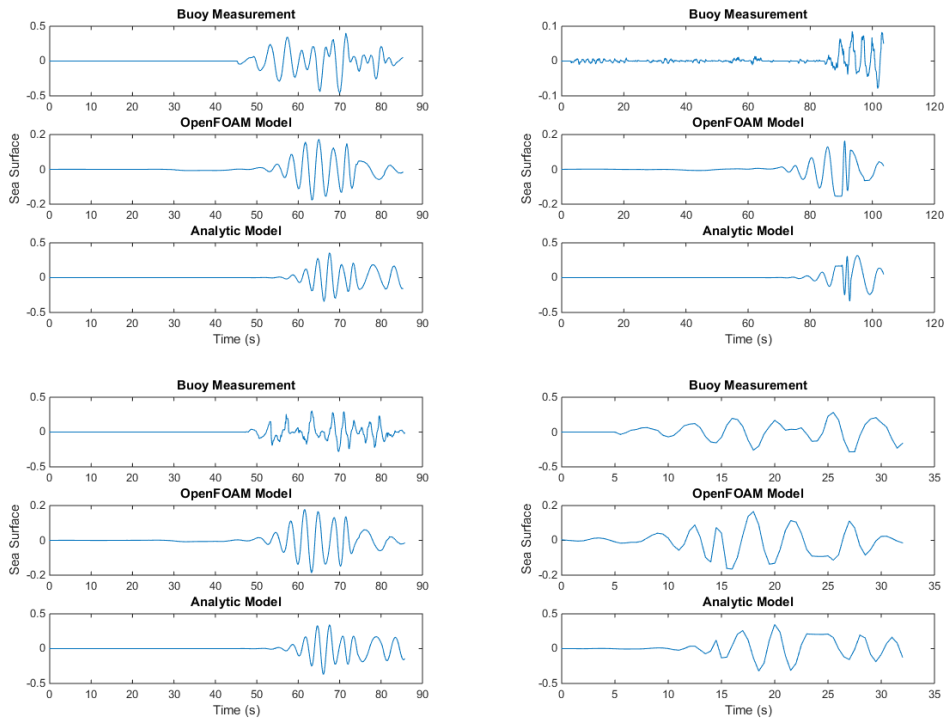


Figure 47: Lagrangian tracking comparisons. Note that the OpenFOAM model tends to underestimate the sea surface.

## 7 Conclusions

### 7.1 Summary

The wakes produced by Issaquah and Super Class WSF vessels were studied using an array of GPS buoys, a Navier-Stokes computational model using the CFD code OpenFOAM, and with an analytic potential flow wake model. Each of these methods produced results that indicate a maximum wake height for a given distance from the sailing line of the vessel and a given vessel speed. These results are summarized in Fig. 46. The in-situ buoy measurements are regarded to be the most reliable, but also the contain the most sparse data. Computational results suffered from numerical dissipation and tend to underestimate wake height and overestimate wake decay. The transverse wake structure, however, is well-captured (see Table 1). The analytic model relies on a very primitive proxy for the real vessel hull, and therefore requires experimental knowledge to properly tune the model. Once tuned, the analytic model closely recreates the observed wake structure.

### 7.2 Vessel Speed Recommendations

Field data indicate a clear difference in peak wake height between the various operating speeds of Issaquah class vessels. The lower vessel speed ranges of 10.5–11 knots and 13.3–14.2 knots produce nearly identical wake profiles. Some of this effect may be due to ocean currents, however. At the higher speed range of 17.3–18.2 knots, the Issaquah class vessels produce significantly higher wakes, at all distances from the sailing line. Analytic data indicate a roughly linear relationship between peak wake height at a given distance from the sailing line and vessel speed in the regime of interest. Therefore, in assessing a given distance and peak height objective, the field data plots should be used as two data points, with a linear interpolation to determine appropriate speed.

### 7.3 Conclusions from Modeling

The OpenFOAM model shows promise for further development into a larger, higher resolution simulation. However, significant computation time would be required- on the order of  $10^4$ – $10^5$  CPU hours are recommended for future model simulations. The analytical model was shown to be useful in determining basic scaling and trends for vessel speed and rough shape, and was quite computationally efficient. The analytic model was ultimately able to recreate the difference in performance between the Issaquah and Superclass vessels observed in 6.1.

### 7.4 Possible Extensions and Future Work

Ocean current and wind conditions are known to be confounding factors in how wakes propagate. Currents are particularly important when ferry transit is con-

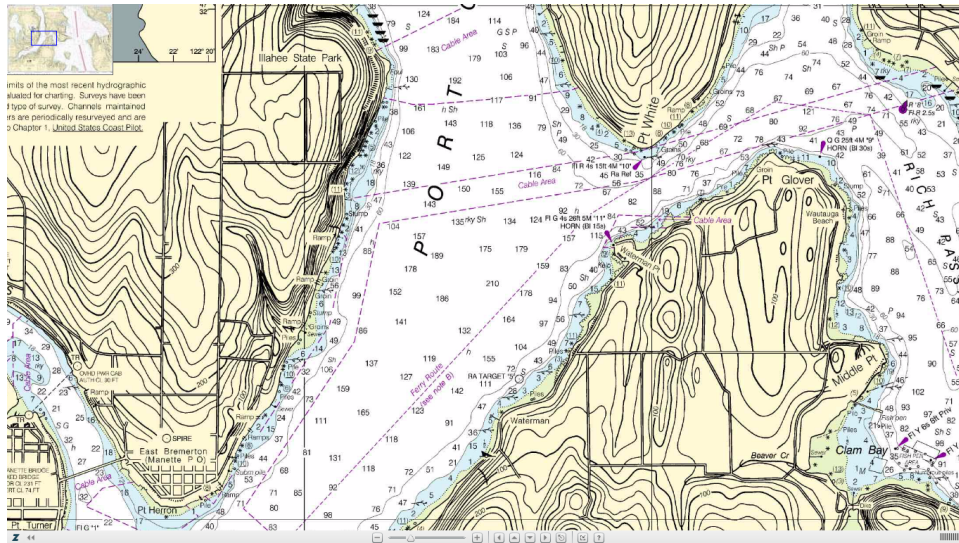
sidered, since the vessel desires to maintain speed over ground, rather than speed relative to the sea surface. While the buoys themselves are insufficient to create a useful current map of the region, their GPS tracks while free floating would be used as Lagrangian surface trackers for validating an ocean current model.

## 8 Acknowledgements

Funding for this work was provided by the Washington State Department of Transportation. The prior and ongoing work of Golder and Associates (see [3]) was instrumental as a reference in designing and planning field work and data analysis. Technical support was provided by Joe Talbert and Alex de Klerk of UW's Applied Physics Lab. The Aquadopp testing was carried out just offshore of the property owned by Bill Cairn, with his gracious permission. Finally Andrew Reay-Ellers served as the captain of the R/V Jack Robertson during field work.

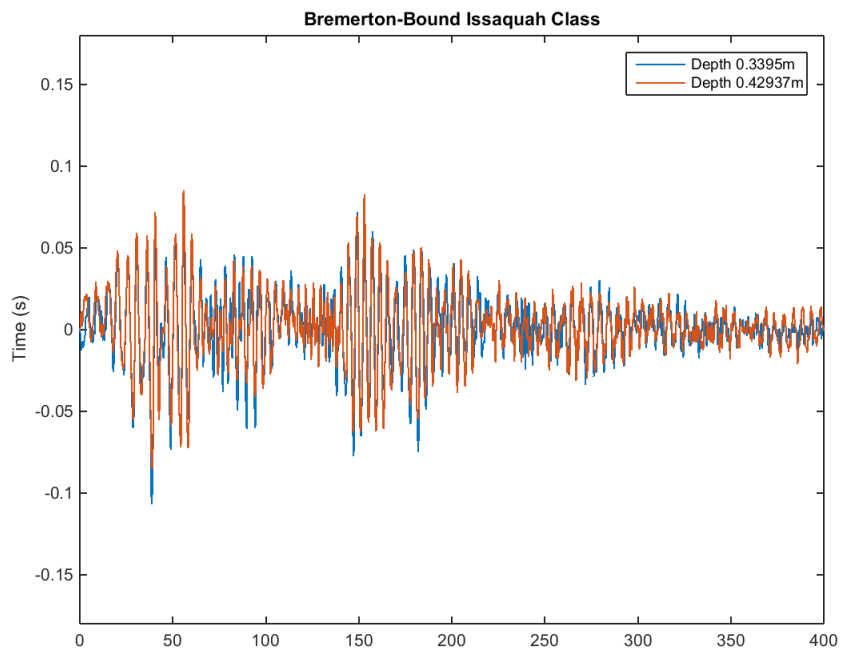
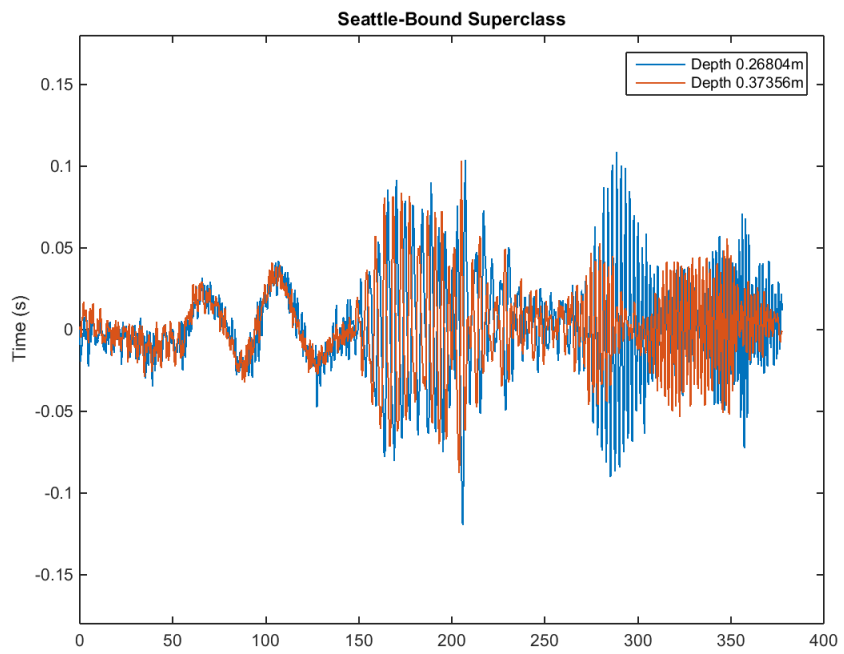
## 9 Appendix

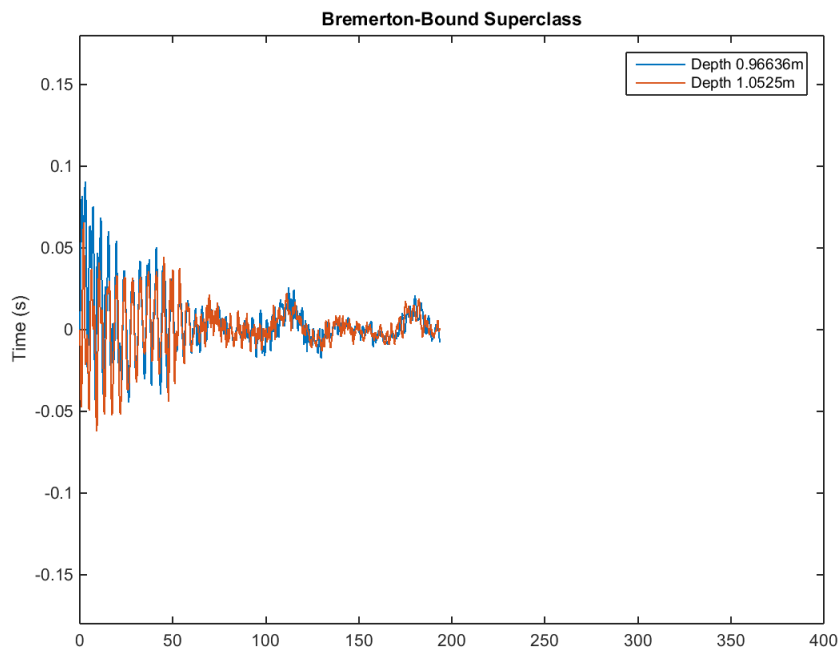
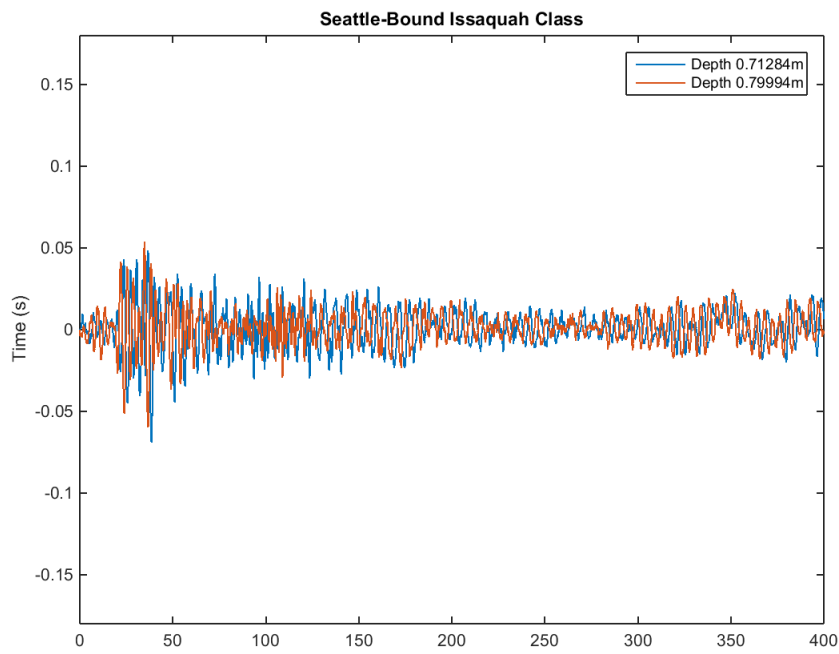
### 9.1 Rich Passage Depth Chart

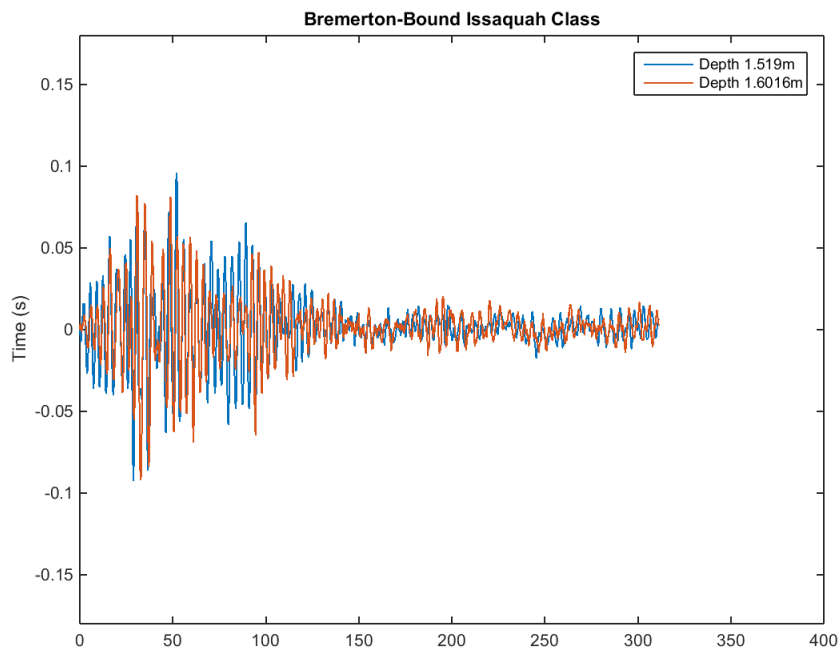
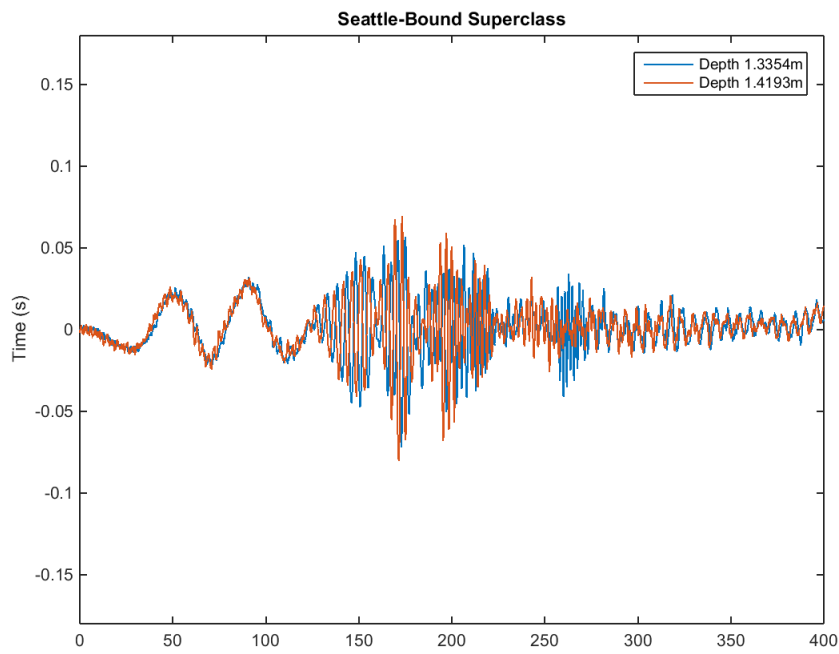


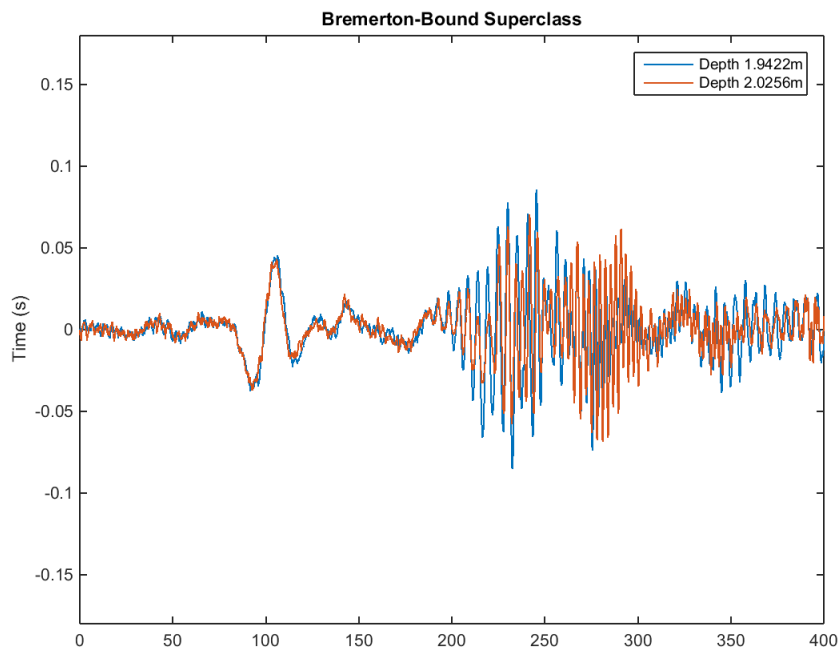
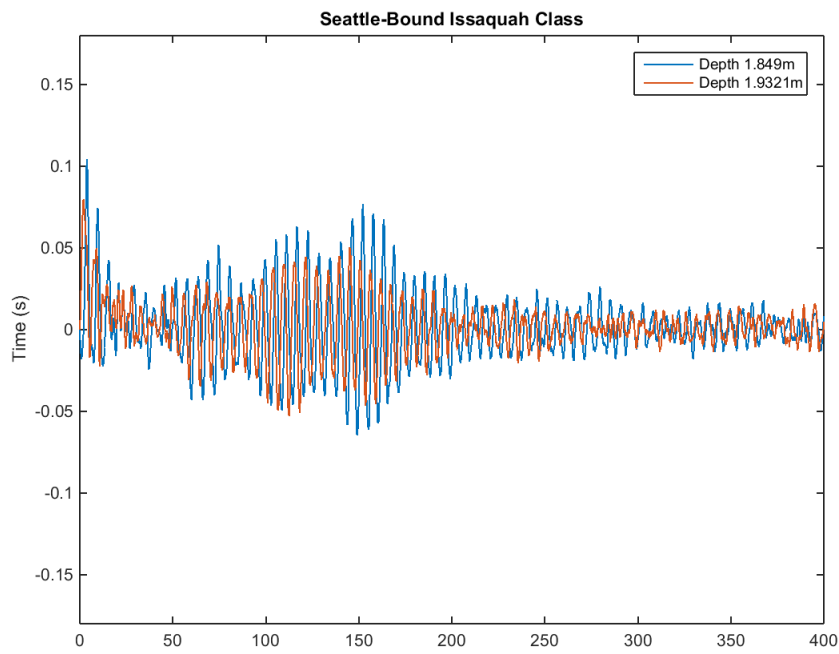
### 9.2 Processed Pressure Gauge Data

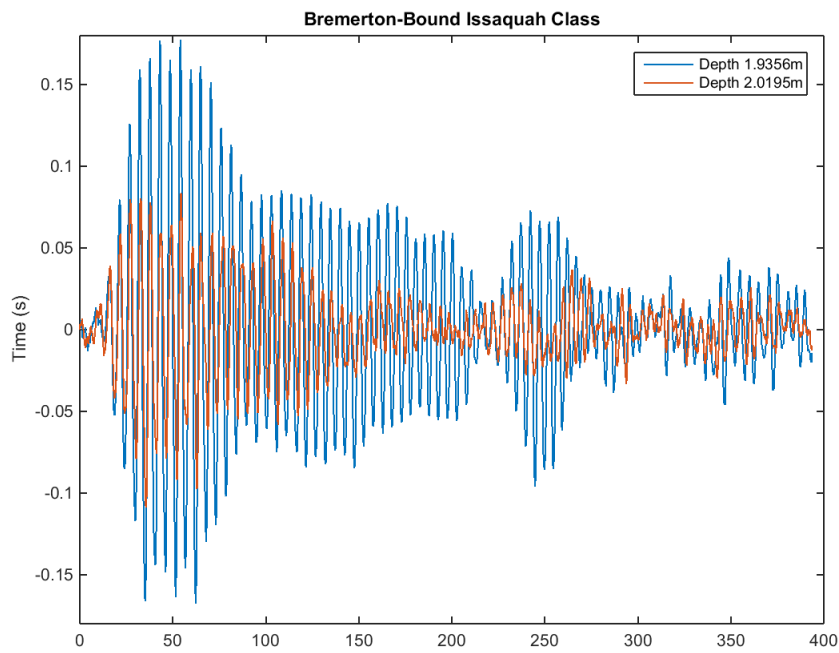
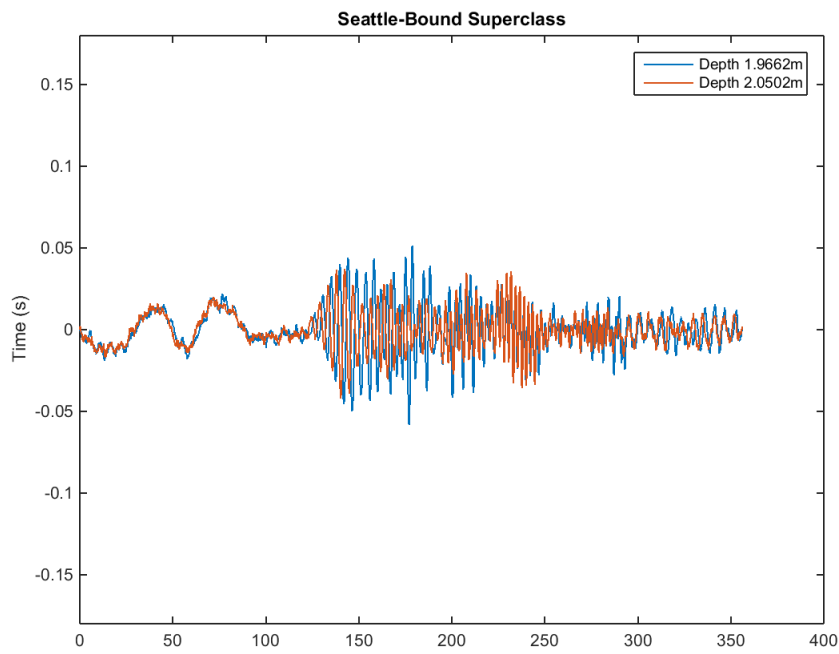
Note: on the fourth and seventh plot below, the beginning of the wake event was not captured by the Aquadopp. The plot represents the earliest available data.



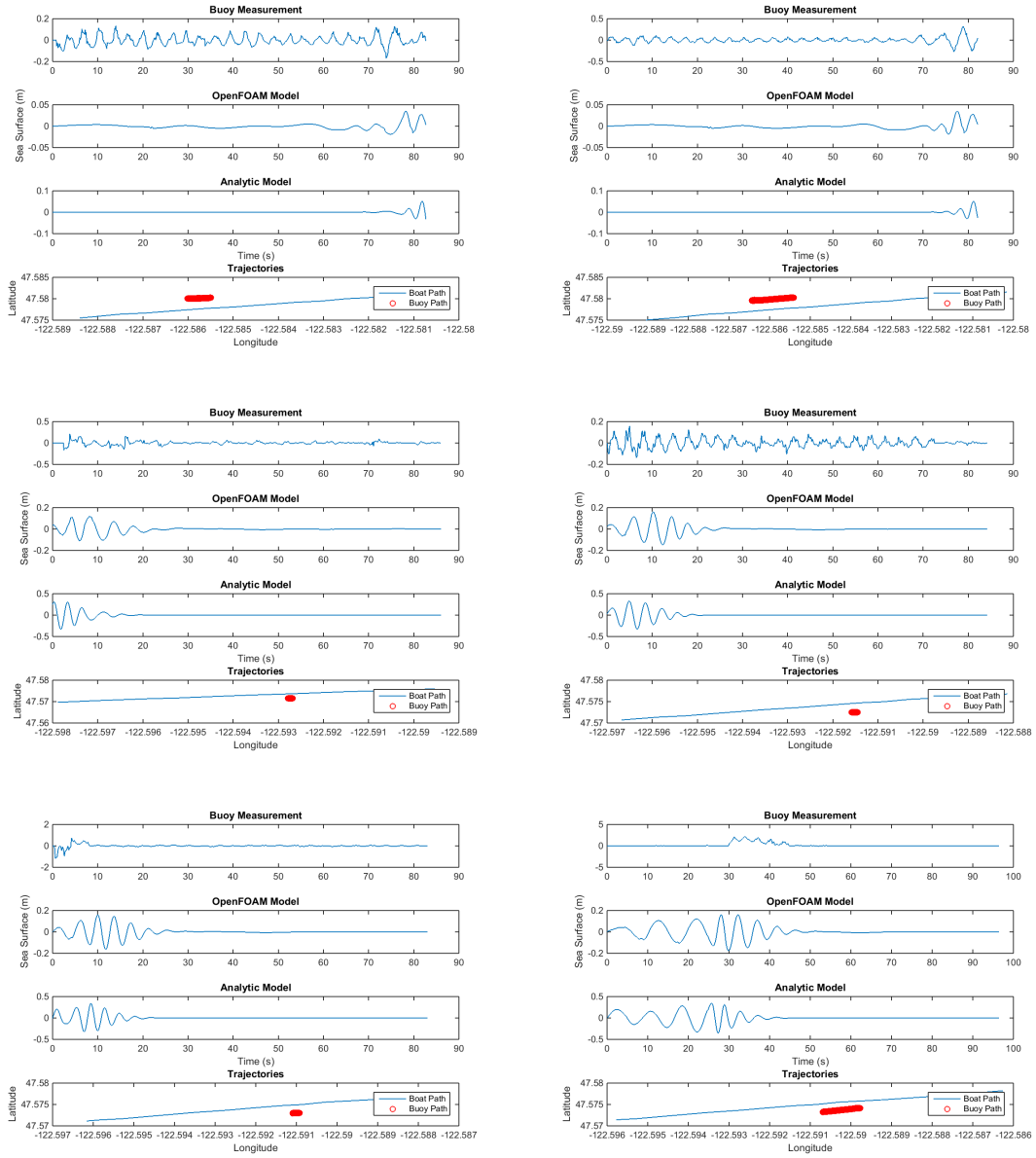


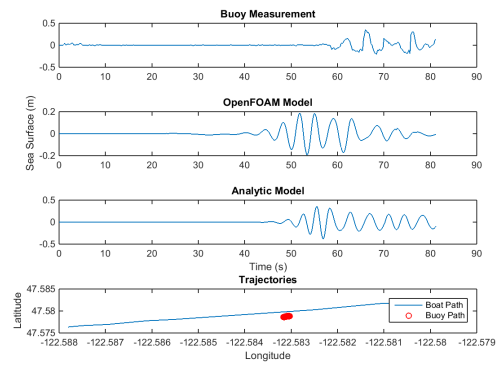
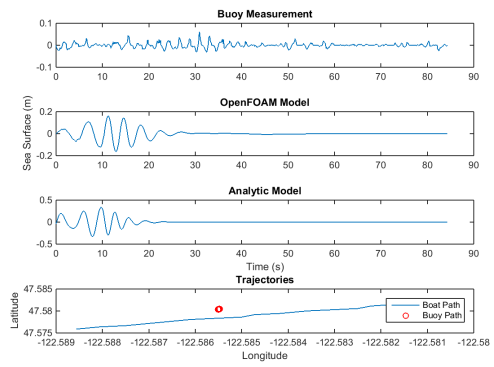
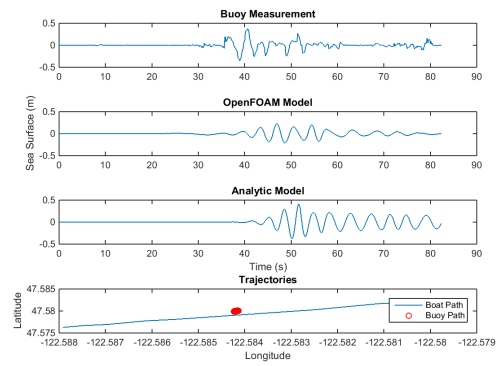
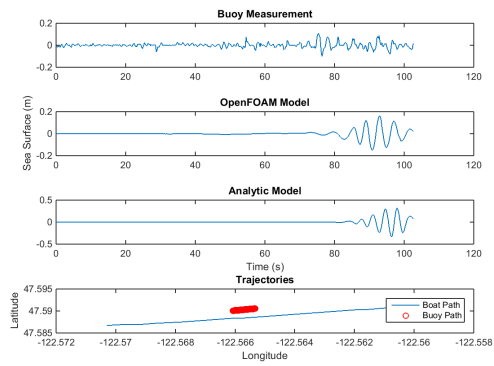
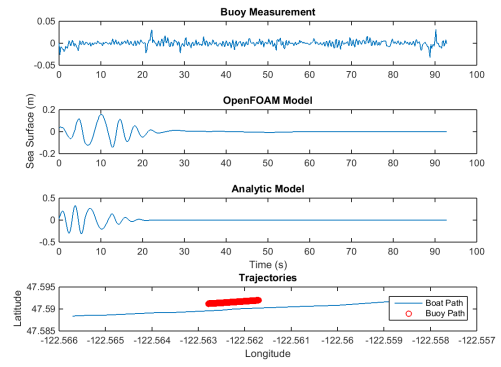
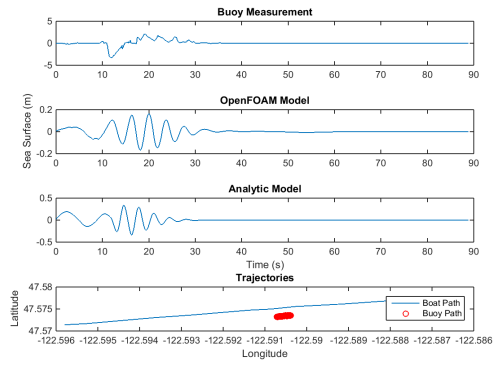


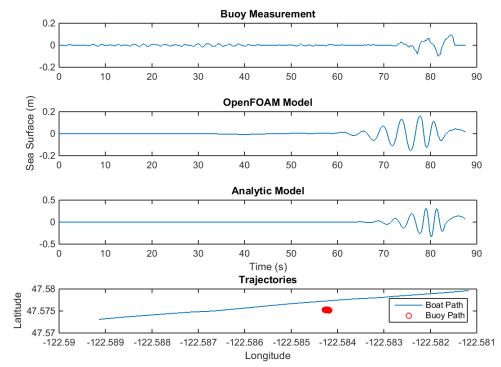
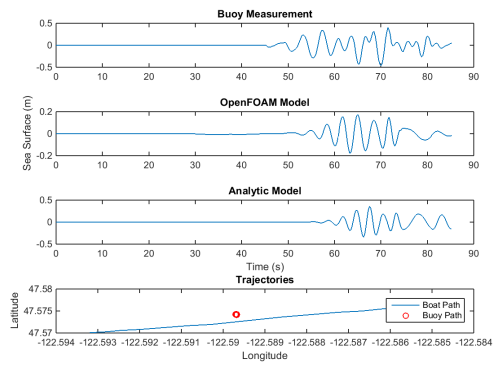
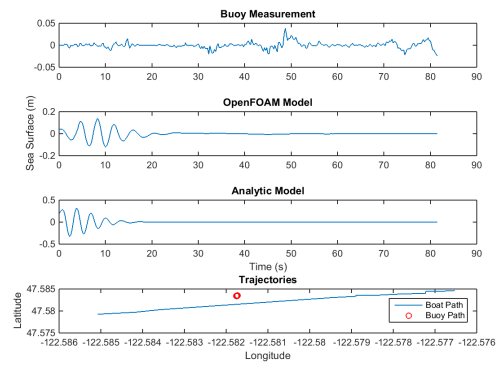
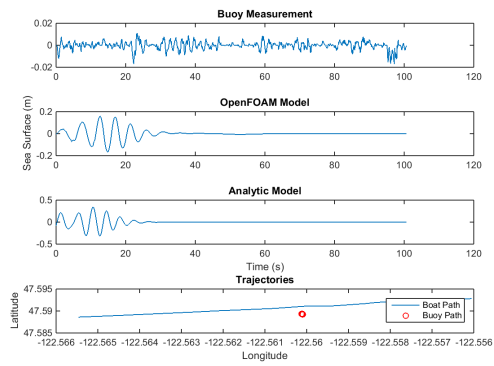
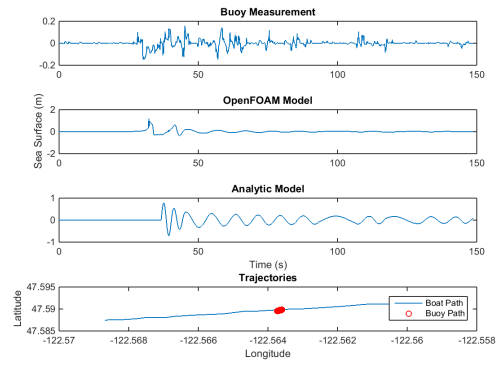
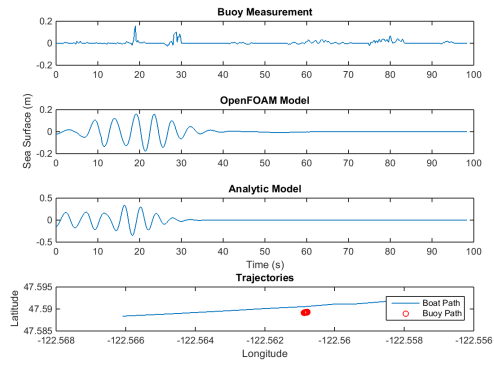


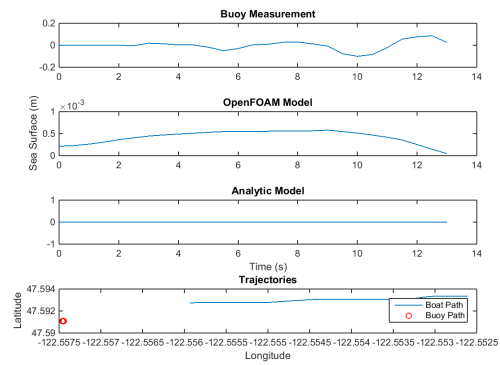
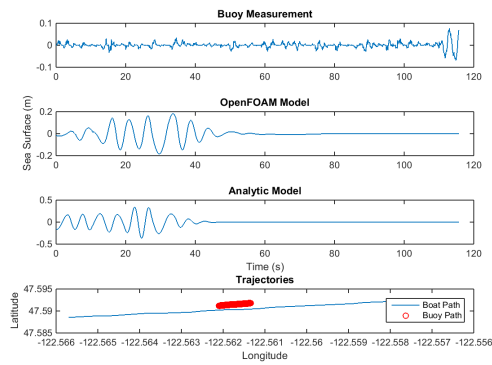
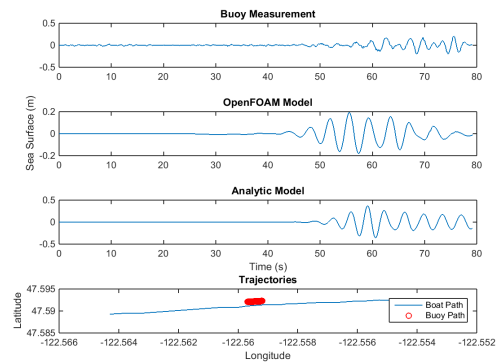
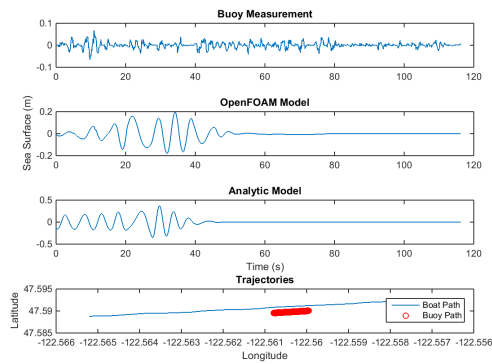
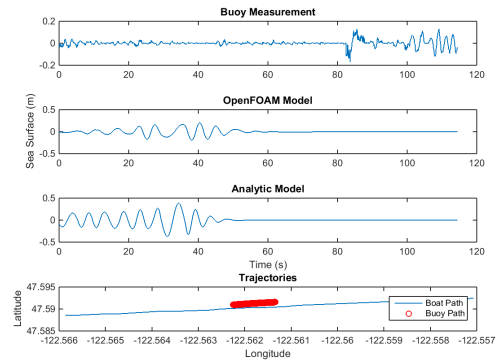
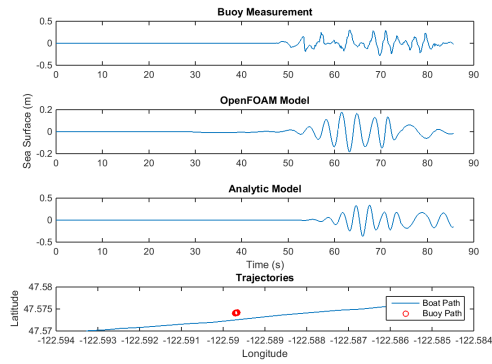


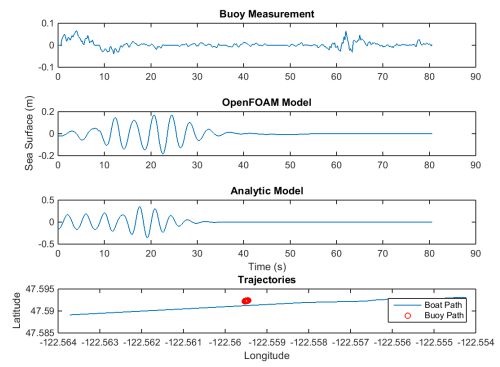
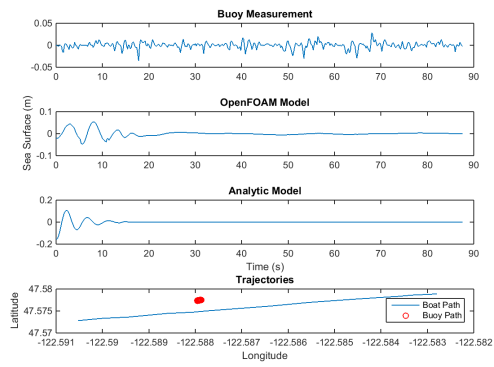
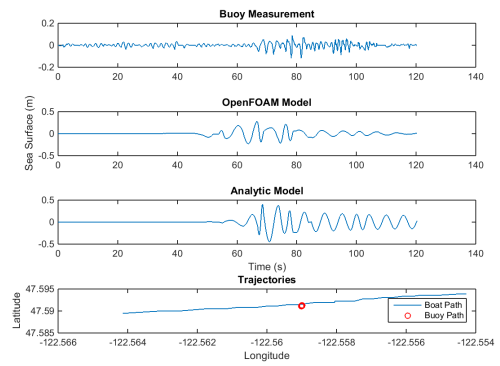
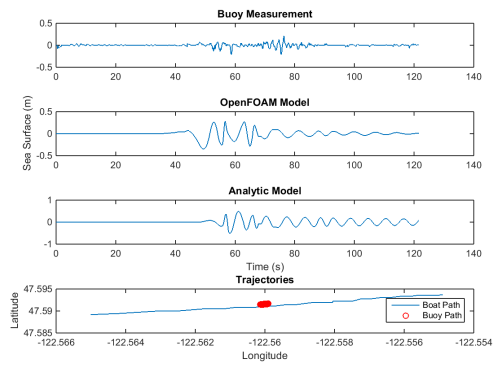
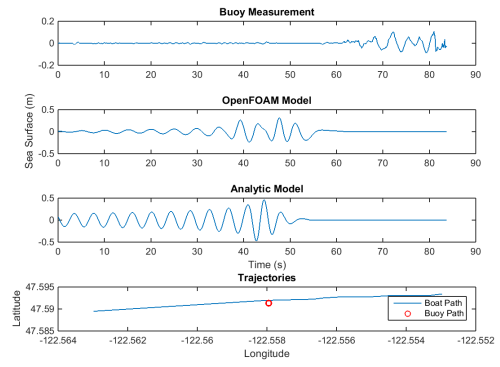
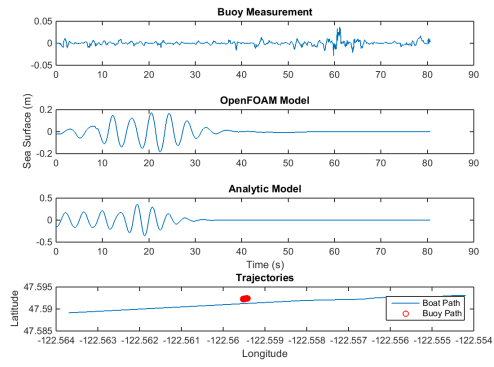
### 9.3 Lagrangian Tracking Comparison Plots

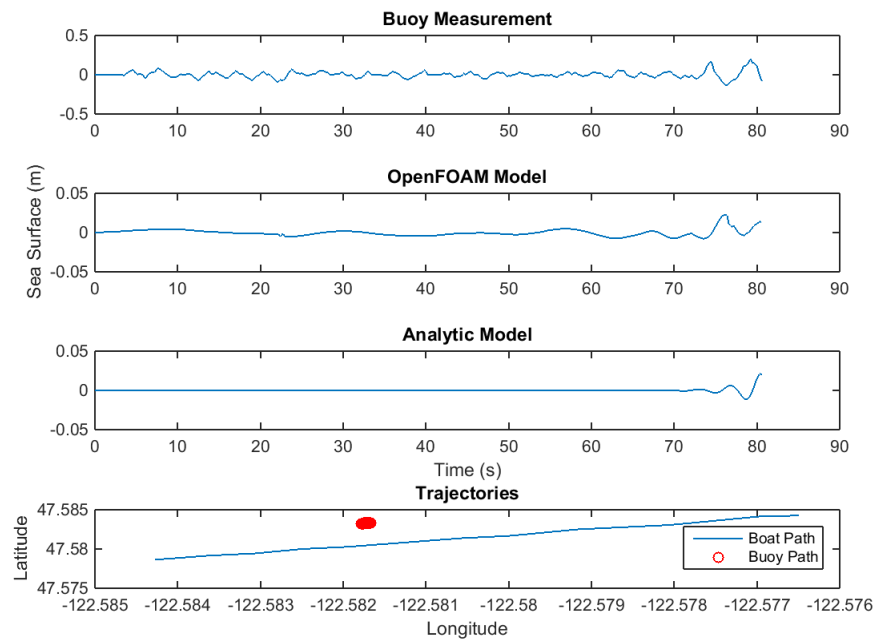
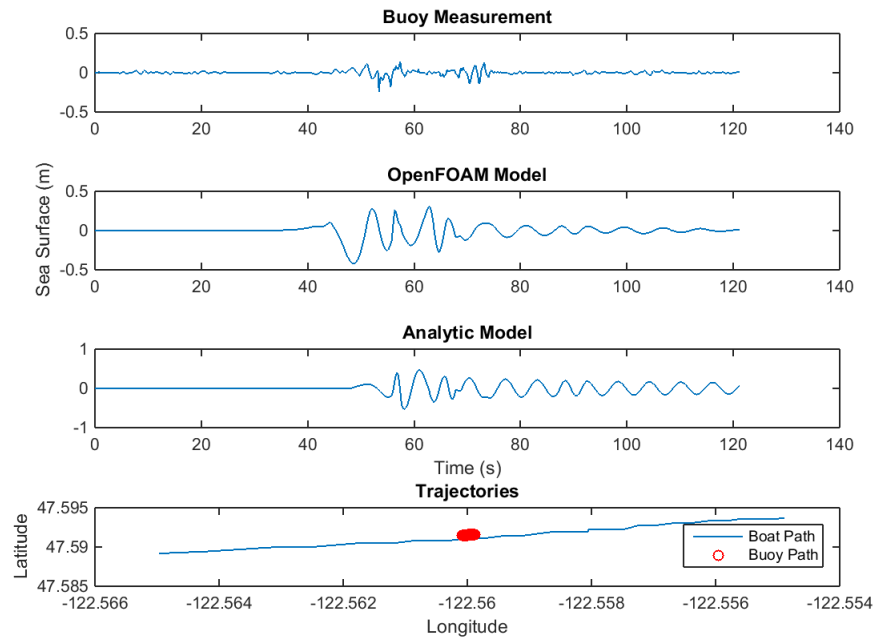












## 9.4 Statistical Methods

Methods below are based on the formalism and theory developed in Spectral Analysis for Physical Applications, by Donald Percival.

The periodogram is defined by

$$S(f) = \Delta_t \sum_{\tau=-\infty}^{\infty} \text{cov}\{X_{t+\tau}, X_t\} e^{-2\pi i f \tau \Delta_t}$$

for a time series  $X_t$  with sampling period  $\Delta_t$

To deal with the noisiness of the periodograms, it is natural to use a lag window estimator. Such an estimator is given as

$$S^{(LW)}(f) = \int_{-f_N}^{f_N} V_m(f - \phi) S^{(P)}(\phi) d\phi$$

where  $V_m(f)$  is the Fourier transform of a Gaussian function  $e^{-t^2/m^2}$  and  $f_N$  is the Nyquist frequency.

Using prior knowledge about the expected SDF, a peak bandwidth

$$B_W \equiv \frac{1}{\int_{f_N}^{f_N} V_m^2(f) df} \approx 0.4$$

can be assumed. Solving for  $m$  yields the result of  $m = 20$  being the optimal choice. Compared to the periodogram, the smoothing provides a much better visual representation of the SDF.

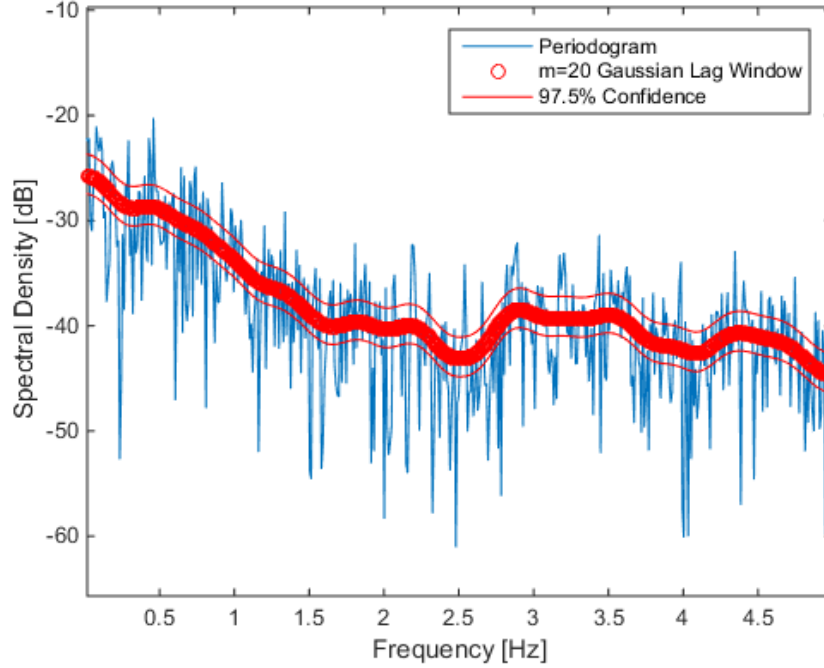


Figure 48: A typical single periodogram with a Gaussian lag window estimator overlaid. Setting  $m=20$  captures peaks of width 0.4 Hz and larger. The EDOF for this estimate is 42.03

For the aggregate SWIFT measurements it becomes useful to average over many spectral estimators and obtain confidence intervals based on a  $\chi^2$  distribution. The equivalent degrees of freedom for a combination of Gaussian lag window estimators is developed as follows:

For a direct spectral estimator,

$$\hat{S}^{(D)}(f) \doteq S(f) \frac{\chi_2^2}{2}$$

at well-behaved frequencies. And the combined direct spectral estimator is

$$\sum_{n=1}^N \hat{S}^{(D)}(f) \doteq \sum_{n=1}^N S(f) \frac{\chi_2^2}{2} \doteq S(f) \frac{\chi_{2N}^2}{2N}$$

When the SDF estimators that we are combining have  $\nu_n$  EDOFs, then this expression is revised to

$$\sum_{n=1}^N \hat{S}^{(\text{lag})}(f) \doteq \sum_{n=1}^N S(f) \chi_{\nu_n}^2 / 2 \doteq S(f) \chi_{\sum \nu_n}^2 / (2N)$$

For constant  $\nu_n = \nu$  as in this case, we can revise the estimate to

$$\sum_{n=1}^N \hat{S}^{(\text{lag})}(f) \doteq S(f) \chi_{N\nu}^2 / (2N)$$

With this method (which is only valid for independent observations), we can achieve a very tight confidence interval using relatively few samples. A judicious choice of  $m$  can increase the EDOFs by an order of magnitude or more.

## References

- [1] Appel, W., *Mathematics for Physics and Physicists*. Princeton University Press. (2007).
- [2] Benzaquen, M., Darmon, A., and Raphael, E., "Wake pattern and wave resistance for anisotropic moving disturbances", *Physics of Fluids*. 2014.
- [3] Cote, J., Curtiss, G., and Osborne, P. "Rich Passage 1 Wake Validation and Shore Response Study". *Ports 2013*: **225-234**. (2013).
- [4] Dossett, Jake. "Analyzing Washington State Car Ferry Wakes". (2014).
- [5] Darmon, A., Benzaquen, M., and Raphael, E., Kelvin wake pattern at large froude numbers, *J. Fluid Mech.* **738**, R3 (2014).
- [6] Farley, J., Friedrich, E. "Is Bremerton Fast Ferry's Economic Wake worth a Tax Hike?" *BSUN. Kitsap Sun*, 10 Mar. 2013.
- [7] Herbers, T.H.C, P. F. Jessen, T. T. Janssen, D. B. Colbert, and J. H. MacMahan. "Observing Ocean Surface Waves with GPS-Tracked Buoys". *J. Atmos. Oceanic Technol.*, 29, **944-959**. (2012).
- [8] Menter, F. R. "Two-Equation Eddy-Viscosity Turbulence Models for Engineering Applications", *AIAA Journal* 32 (8): **1598-1605**. (1994)
- [9] Nece, Ronald, Michael McCaslin, and D. R. Christensen. "Ferry Wake Study". Rep. N.p.: Washington State Department of Transportation. (1985).
- [10] Nortek AS. "Aquadopp Current Profiler User Guide". Tech. no. N3009-103. (2008).
- [11] Percival, Donald B., and Andrew T. Walden. *Spectral Analysis for Physical Applications: Multitaper and Conventional Univariate Techniques*. Cambridge: Cambridge UP, 1993.
- [12] Stoker, J. J. *Water Waves; the Mathematical Theory with Applications*. New York: Interscience. (1957).

- [13] Smith, Benjamin, WSF Service Planning Manager. "It's A Boat, Its A Train It's Super-Transit!" Multimodal Operations Planning Workshop, Seattle. (2013).
- [14] Thomson, J. "Wave Breaking Dissipation Observed with SWIFT Drifters". J. Atmos. Oceanic Technol., 29, **1866-1882**. (2012).
- [15] Thomson, William, On the waves produced by a single impulse in water of any depth, Proc. R. Soc. London, Ser. A42, **80-83** (1887).